Journal of Computational Physics 228 (2009) 4118–4145

Contents lists available at ScienceDirect

Journal of Computational Physics

journal homepage: www.elsevier.com/locate/jcp

# Compact third-order limiter functions for finite volume methods

Miroslav Čada *, Manuel Torrilhon

*Seminar for Applied Mathematics, ETH Zentrum, CH-8092 Zurich, Switzerland*

ARTICLE INFO

*Article history:*
Received 16 January 2008
Received in revised form 9 January 2009
Accepted 15 February 2009
Available online 28 February 2009

*Keywords:*
Numerical methods
Conservation laws
Finite volume methods
High-order accuracy
Shock capturing
Non-linear and non-polynomial limiter

ABSTRACT

We consider finite volume methods for the numerical solution of conservation laws. In order to achieve high-order accurate numerical approximation to non-linear smooth functions, we introduce a new class of limiter functions for the spatial reconstruction of hyperbolic equations. We therefore employ and generalize the idea of double-logarithmic reconstruction of Artebrant and Schroll [R. Artebrant, H.J. Schroll, Limiter-free third order logarithmic reconstruction, SIAM J. Sci. Comput. 28 (2006) 359-381].

The result is a class of efficient third-order schemes with a compact three-point stencil. The interface values between two neighboring cells are obtained by a single limiter function. The limiter belongs to a family of functions, which are based upon a non-polynomial and non-linear reconstruction function. The new methods handle discontinuities as well as local extrema within the standard semi-discrete TVD-MUSCL framework using only a local three-point stencil and an explicit TVD Runge–Kutta time-marching scheme. The shape-preserving properties of the reconstruction are significantly improved, resulting in sharp, accurate and symmetric shock capturing. Smearing, clipping and squaring effects of classical second-order limiters are completely avoided.

Computational efficiency is enhanced due to large allowable Courant numbers (CFL $\lesssim 1.6$), as indicated by the von Neumann stability analysis. Numerical experiments for a variety of hyperbolic partial differential equations, such as Euler equations and ideal magneto-hydrodynamic equations, confirm a significant improvement of shock resolution, high accuracy for smooth functions and computational efficiency.



## 1. Introduction

In the present paper we will derive a new third-order method for the computation of numerical fluxes within the framework of finite volume (FV) schemes for conservation laws. FV methods, in general, are derived from the integral formulation of conservation laws for a spatial domain $\Omega$ and a quantity $\boldsymbol{u}$

$$\frac{\mathrm{d}}{\mathrm{d}t}\int_{\Omega}\boldsymbol{u}(x,t)\,\mathrm{d}x = -\int_{\partial\Omega}\boldsymbol{f}(\boldsymbol{u}(x,t))\cdot\boldsymbol{n}\,\mathrm{d}S. \tag{1.1}$$

The volume of $\boldsymbol{u}$ can only change in time by the dynamics of the flux $\boldsymbol{f}(\boldsymbol{u}(x,t))$ across the boundary $\partial\Omega$.

Solutions to these equations have typically smooth structures interspersed with discontinuities. An accurate prediction of such interactions is of importance in many computational fluid dynamic (CFD) applications, such as aircraft design, stellar formation, and weather simulations, to name only a few. The main task is to develop algorithms that ensure the conservation property Eq. (1.1), that are highly accurate for smooth regions in both time and space, and that have sharp transition where large gradients or discontinuities appear.

* Corresponding author.
*E-mail addresses:* cada@math.ethz.ch (M. Čada), matorril@math.ethz.ch (M. Torrilhon).

0021-9991/$ - see front matter © 2009 Elsevier Inc. All rights reserved.
doi:10.1016/j.jcp.2009.02.020

Numerical methods for conservation laws can in general be divided into two approaches: a one-step approach, where time and space discretization is coupled via the Cauchy–Kowalewski procedure (see e.g. [15,27]) and semi-discrete schemes, where time and space integration are separated. The latter has been a very successful approach towards the dual objective, i.e., high accuracy and non-oscillatory transitions. It uses strong stability preserving Runge–Kutta time-marching schemes, combined with polynomial reconstruction of the interface value $\boldsymbol{u}(x,t)|_{\partial\Omega}$ of the flux $\boldsymbol{f}(\boldsymbol{u}(x,t)|_{\partial\Omega})$ from a given cell average.

One of the first high-order semi-discrete algorithm was van Leer's TVD-MUSCL (Monotonic Upstream-centered Scheme for Conservation Laws) scheme [19]. A piecewise-linear spatial approximation was combined with a second-order time integration. To avoid spurious oscillations total variation diminishing (TVD) limiters were used. TVD limiters are bounded non-linear functions obeying Harten's TVD conditions [8]. These limiters ensure that any reconstructed values at any time do not lie outside the range of the initial data, thus precluding accurate resolution of local extrema. To avoid this drawback, Harten et al. [9] later introduced the concept of essentially non-oscillatory (ENO) schemes. ENO methods use instead of a non-linear limiter an optimal stencil search procedure, which chooses the locally "smoothest" reconstruction, thereby avoiding interpolation across discontinuities. Due to the adaptive stencil, the finally approximated interface value does not consist of all available data. In the weighted ENO (WENO) scheme by Liu et al. [17] the interface values are computed as convex combinations of all candidate stencils, hence making better use of the available data. In contrast to TVD schemes both ENO and WENO methods introduce spurious yet bounded variation, which eventually decreases as the mesh is refined.

At the same time the idea of limiting has been further developed as extensions of the TVD-MUSCL scheme. A third-order method was developed by Woodward and Colella [36]. They used a four-point centered stencil to recover the interface values, which afterwards were limited in the vicinity of a discontinuity. An even higher-order extension was introduced by Suresh and Huynh [26] employing a five-point stencil reconstruction with a limiting procedure, which preserves monotonicity and accuracy for smooth extrema, easing the TVD constrain. To apply the costly limiting routine efficiently, they preprocess the data to localize discontinuities. Waterson and Deconinck [34] have recently presented a unified classification of limiters based on three-points. A successful limiter in this family is the Koren limiter [13] (see also [2]). All analyzed limiter functions were derived from polynomial reconstruction functions and degenerated to first-order for smooth extrema.

In contrast to the method based upon a polynomial approximation of the interface values, Artebrant and Schroll [5] have recently developed a new non-polynomial reconstruction function. Originally motivated by the work of Marquina [18], who used a hyperbola as reconstruction function, they recover the interface values with a local double logarithmic (LDLR) Ansatz function. Due to the logarithmic nature it is able to handle discontinuities without spurious oscillations, yet introducing local bounded variation. In contrast to Marquina's hyperbolic reconstruction LDLR can recover local extrema without loss of accuracy. It is local, in the sense that it uses only a three-point stencil and it does not use classical limiters to avoid oscillations. Numerical experiments in [5] indicate its superior performance compared to other third-order methods and reconstruction techniques.

Inspired by the results of Artebrant and Schroll [5] we have followed a different path. The local and symmetric nature of LDLR allowed a simpler, yet more efficient formulation of Artebrant and Schroll's scheme, thus resembling very much van Leer's three-point TVD-MUSCL algorithm using only a single limiter function. Furthermore this interpretation not only simplified the original reconstruction, but also improved its shock capturing qualities and reconstruction efficiency without the application of a logarithmic function at all. This eventually led to a whole family of limiter functions, which recover smooth extrema with third-order accuracy. We want to emphasize that the paradigm of this paper is to rigorously restrict the limiting procedure to a three-point stencil. Consequently we have to cope with the problem of recovering discretized smooth structures with few data points. Yet, we remain in the well-understood context of the efficient classical TVD-MUSCL scheme. Taking into account that the proposed limiters are simple $(\max -, \min -)$ functions, which do not expand the computational stencil, they become attractive candidates to be easily incorporated into already existing TVD codes.

To emphasize the close relation of the proposed third-order limiting method with van Leer's TVD-MUSCL scheme, we first revisit the second-order one in Section 2. In Section 3, the main properties of the new limiter functions – the key features of our scheme – its connection and the differences to LDLR and other schemes will be explained. Furthermore the difficulty of recovering local extrema with a three-point stencil without loss of accuracy will be discussed and solved. In order to reach a overall third-order accuracy we use the explicit three-stage TVD Runge–Kutta time integration of Gottlieb and Shu [7]. In Section 4 we investigate the characteristic properties of the new methods in the frequency domain, in terms of a linear von Neumann stability analysis. Convergence studies and various numerical experiments, including one- and two-dimensional systems appear in Section 5. Finally conclusions are presented in Section 6.

## 2. Spatial reconstruction: standard TVD-MUSCL methods

For simplicity and in order to settle our notation we consider the numerical approximations to the one-dimensional scalar initial value problem

$$\begin{aligned} u_t &= -f(u)_x, \\ u(x, t=0) &= u_0(x), \end{aligned} \tag{2.1}$$

where $u_0$ is either a piecewise smooth function with compact support or a periodic function. Note that the flux in Eqs. (1.1) and (2.1) appears on the right-hand side to emphasize the semi-discrete formulation. We cover the uniform computational

region with control cells $C_i^n = [x_{i-\Delta x/2}, x_{i+\Delta x/2}] \times [t^n, t^{n+1}]$, with $t^{n+1} = t^n + \Delta t$ and the computational grid $x_{i\pm1} = x_i \pm \Delta x$. Integrating the conservation law Eq. (2.1) over the control volume $C_i$, we obtain the standard finite volume (FV) update

$$\frac{\mathrm{d}}{\mathrm{d}t}\bar{u}_i = L_i(\bar{u}^n) = \frac{1}{\Delta x}\left[\mathcal{F}(\hat{u}^{(-)}_{i-\frac{1}{2}}, \hat{u}^{(+)}_{i-\frac{1}{2}}) - \mathcal{F}\left(\hat{u}^{(-)}_{i+\frac{1}{2}}, \hat{u}^{(+)}_{i+\frac{1}{2}}\right)\right] \tag{2.2}$$

for the cell average $\bar{u}_i^n$ at time $t^n$

$$\bar{u}_i^n = \frac{1}{\Delta x}\int_{x_{i-\Delta x/2}}^{x_{i+\Delta x/2}} u^n(x)\,\mathrm{d}x \tag{2.3}$$

based on the numerical flux function $\mathcal{F}$, which is supposed to be Lipschitz continuous and consistent with the flux $f(u)$:

$$\mathcal{F}(u,\ldots,u) = f(u). \tag{2.4}$$

The evolution of $\bar{u}_i^n$ is governed by the left and right limits $\hat{u}^{(\pm)}_{i+\frac{1}{2}}$ – the interface values – of the reconstructed function $\hat{u}(x)$. The cell interface value $\hat{u}_{i+\frac{1}{2}} = \hat{u}(\bar{u}_i^n, \bar{u}_{i+1}^n)$ denotes the intermediate value at $x_{i+1/2}$ of the Riemann problem solution with initial data $\bar{u}_i^n, \bar{u}_{i+1}^n$. The calculation of the interface values from the known cell mean values is the essential reconstruction task and determines the scheme's order of accuracy. This is the main concern of this paper.

To obtain higher-order accuracy, we have to improve the reconstruction of the left and right limits $\hat{u}^{(\pm)}_{i+\frac{1}{2}}$ and we also have to adjust the time integration by a higher-order time-stepping method. Since we consider a local reconstruction, i.e. a three-point stencil, we define the interface values as

$$\begin{aligned}\hat{u}^{(-)}_{i+\frac{1}{2}} &\equiv L(\bar{u}_{i-1}, \bar{u}_i, \bar{u}_{i+1}),\\ \hat{u}^{(+)}_{i+\frac{1}{2}} &\equiv R(\bar{u}_i, \bar{u}_{i+1}, \bar{u}_{i+2}),\end{aligned} \tag{2.5}$$

where capital $L$ and capital $R$ denote the left and right cell interface approximations, respectively. In order to obtain high-order non-oscillatory reconstructions, the interpolation function Eq. (2.5) is a priori non-linear.

The classical second-order TVD-MUSCL scheme assumes a piecewise-linear interpolation from the average values $\bar{u}_i(t)$.

$$\begin{aligned}\hat{u}^{(-)}_{i+\frac{1}{2}} &= \bar{u}_i + \frac{\Delta x}{2}\sigma_i,\\ \hat{u}^{(+)}_{i-\frac{1}{2}} &= \bar{u}_i - \frac{\Delta x}{2}\sigma_i,\end{aligned} \tag{2.6}$$

where the slope $\sigma$ can either be expressed via upwind, downwind or centered finite differences to recover the Beam-Warming, Lax–Wendroff or Fromm method, respectively (see e.g. [15]).

In order to avoid Gibbs' phenomenon and to control the resulting oscillation, TVD limiters have to be applied directly on the slopes. Hence the reconstructed interface values are expressed in terms of non-linear limiter functions using, e.g. the downwind slope

$$\sigma_i = \left(\frac{\delta_{i+\frac{1}{2}}}{\Delta x}\right)\phi(\theta_i), \tag{2.7}$$

where $\delta_{i+\frac{1}{2}} = \bar{u}_{i+1} - \bar{u}_i$ is the difference across a cell interface, and

$$\theta_i = \frac{\delta_{i-\frac{1}{2}}}{\delta_{i+\frac{1}{2}}}, \quad \delta_{i+\frac{1}{2}} \neq 0 \tag{2.8}$$

is a local smoothness measure.

If the limiter function satisfies $\phi(1+\Delta x) = 1 + \frac{\Delta x}{2} + \mathcal{O}(\Delta x^2)$ for $\bar{u} \in C^\infty$ and is Lipschitz continuous at $\theta = 1$ we recover second-order accuracy in space. Classical TVD-limiter functions, such as minmod, super-bee and monotonized central difference limiter (MCD) (see e.g. [27,15]) lie in the TVD region ($\phi(\theta) - \theta$ plane):

$$\begin{cases} 0 \leqslant \phi(\theta) \leqslant 2\theta,\\ 0 \leqslant \phi(\theta) \leqslant 2.\end{cases} \tag{2.9}$$

This region is a direct consequence of Harten's TVD theorem. For $\theta \leqslant 0$ the reconstruction reduces to the constant cell average itself and smooth extrema for which $\theta \leqslant 0$ holds cannot be recovered accurately. Thus classical second-order TVD schemes are only of second-order away from local extrema and discontinuities. Yet limiter functions that remain inside Harten's TVD region, do not produce any variation in the vicinity of a discontinuity. This property plus their simplicity and efficiency makes them a popular choice for the CFD community. In general limiters can be considered as logical switches. They continuously change from constant to linear reconstruction. The switching argument is the local smoothness measure equation (2.8), which in its simplest form is only the ratio of the left and right slopes. Unfortunately classical second-order TVD limiters suffer from several well-known drawbacks, such as smearing, clipping and squaring effects of the numerical approximation.

## 3. Third-order limiting

In this section we will derive new limiter functions, which are essentially of third-order accuracy and remain in the standard TVD framework. In contrast to classical limiter functions, the proposed limiters are based upon a non-linear and non-polynomial reconstruction technique. In addition we will explain the close affinity of quadratic interpolation and limiter-free local double-logarithmic reconstruction (LDLR) as proposed by Artebrant and Schroll [5].

### 3.1. Compact third-order reconstruction

The TVD-MUSCL scheme adopts a local three-point stencil to get only a linear interpolation for the spatial approximation of a function $g(x)$. However three-data points are sufficient for constructing a unique quadratic interpolation function

$$p_i(x) = a_i + b_i(x - x_i) + \frac{c_i}{2}(x - x_i)^2$$

resulting in a local third-order reconstruction (see e.g [9] for ENO scheme or [31] for MUSCL schemes) of the interface values

$$\begin{aligned} \hat{u}^{(-)}_{i+\frac{1}{2}} &= \frac{5}{6}\bar{u}_i - \frac{1}{6}\bar{u}_{i-1} + \frac{1}{3}\bar{u}_{i+1}, \\ \hat{u}^{(+)}_{i-\frac{1}{2}} &= \frac{5}{6}\bar{u}_i - \frac{1}{6}\bar{u}_{i+1} + \frac{1}{3}\bar{u}_{i-1}. \end{aligned} \tag{3.1}$$

To derive the parameters $a_i, b_i$ and $c_i$, the quadratic function $p_i(x)$, integrated over the cell $C_i = [x_{i-\Delta x/2}, x_{i+\Delta x/2}]$ has to recover the cell average $\bar{u}_i$ itself and its left and right derivatives located at cell interfaces have to be approximated to second order. Similar third-order reconstruction has also been proposed by Agarwal [1] and others. Yet he applied a four-point stencil in a finite-difference upwind scheme to recover $\hat{u}^{(\mp)}_{i\pm\frac{1}{2}}$.

The oscillatory behavior of the reconstruction depends on the function $g(x)$, which has to be reconstructed. Assume that $g(x)$ is a smooth function on a spatial domain including the finite control volume $C^n_i = [x_{i-\Delta x/2}, x_{i+\Delta x/2}] \times [t^n, t^{n+1}]$ for all times. Suppose that the lateral derivatives are bounded functions of $\mathcal{O}(\Delta x)$. The total variation inside the control cell for both linear and quadratic reconstruction is then

$$TV(p_i(x)) = \int_{x_{i-1/2}}^{x_{i+1/2}} |p_i'(x)|\,\mathrm{d}x = \mathcal{O}(\Delta x). \tag{3.2}$$

If the function $g(x)$ is discontinuous inside the control volume $C^n_i$ for any time, one of the lateral derivatives is an unbounded function of $\mathcal{O}(1/\Delta x)$ and the total variation reads

$$TV(p_i(x)) = \mathcal{O}(1). \tag{3.3}$$

Thus to avoid oscillation in the presence of discontinuities we have to either find a different, yet less oscillatory approximation function $r_i(x)$, or apply limiters, which diminish the total variation in the vicinity of discontinuities. Since we prefer the second approach, we seek to reformulate Eq. (3.1) in a similar way to Eq. (2.6) using suitable limiters, whose accuracy does not degenerate at local extrema.

### 3.2. Logarithmic limiter

Motivated by the work of Marquina [18] on local non-polynomial reconstruction functions, Artebrant and Schroll [5] have recently developed a local double-logarithmic reconstruction (LDLR) using the Ansatz function

$$l_i(x) \sim A_i + B_i \ln(x - x_i + C_i) + D_i \ln(x - x_i + E_i) \tag{3.4}$$

to approximate the interface values. Identically to the construction of a unique parabola equation (3.1) one can construct a local function $l_i(x)$ with uniquely defined values $A_i, B_i, C_i$ and $D_i$.

The LDLR is, in contrast to Marquina's hyperbolic reconstruction, essentially of third-order away from discontinuities without the explicit use of limiters. Due to the logarithmic nature its total variation scales, in the presence of jump discontinuities, with $\mathcal{O}(\Delta x^q |\ln(\Delta x)|)$ [5]. Hence LDLR recovers the cell mean value itself as the mesh is refined. The exponent $q$ will be discussed later. Still a local smoothness measure as argument of the logarithm has to be built in.

Since LDLR is local and uses only three data points, it turns out that the whole reconstruction procedure can be significantly simplified and written in a convenient limiter formulation. The complete derivation is shown in Appendix A.

After some algebraic reformulation we find

$$\begin{aligned} \hat{u}^{(-)}_{i+\frac{1}{2}} &= \bar{u}_i + \frac{1}{2}\phi(\theta_i)\delta_{i+\frac{1}{2}}, \\ \hat{u}^{(+)}_{i-\frac{1}{2}} &= \bar{u}_i - \frac{1}{2}\phi(\theta_i^{-1})\delta_{i-\frac{1}{2}}. \end{aligned} \tag{3.5}$$

This formulation uses only a single limiter function

$$\phi(\theta_i) = \frac{2p((p^2 - 2p\theta_i + 1)\ln p - (1-\theta_i)(p^2-1))}{(p^2-1)(p-1)^2} \tag{3.6}$$

with

$$p = p(\theta_i, q) = 2\frac{|\theta_i|^q}{1+|\theta_i|^{2q}}. \tag{3.7}$$

In contrast to the TVD-MUSCL scheme, we have to use the limiter also with inverse input and hence also with reverse slopes $\delta_{i+\frac{1}{2}}$ (compare $\hat{u}^{(+)}_{i-\frac{1}{2}}$ in Eqs. (3.5) and (2.5). This optimizes the use of the local stencil in the TVD-MUSCL framework, resulting in a third-order accuracy away from discontinuities. The exponent $q$ in Eq. (3.7) controls the amount of the total variation of the reconstruction. It also appears as an exponent in the convergence estimate of the total variation of LDLR at jump discontinuities.

The limiter function Eq. (3.6) has three removable, yet important singularities at $p(\pm 1) = 1$ and $p = 0$. The first two can be removed by setting $\phi(1) = 1$ and $\phi(-1) = \frac{1}{3}$. This ensures that accuracy is not degenerated at local extrema for which $\theta = \pm 1$ holds. Note that the log-limiter Eq. (3.6) itself is not capable of accurately recovering smooth extrema, due to its singularities. This is also the case in the original LDLR algorithm, where Artebrant and Schroll [5] recommended to interpolate around the singularities using three data points, thus a parabola. This interpolation would also lead to $\phi(0) = 0$ at $p = 0$.

The shape of the log-limiter function $\phi(\theta)$ is shown in Fig. 1 for different values of $q$. For

$$q \to 0, \quad p(\theta) \to 1 \quad \forall \theta \in \mathbb{R} \setminus \{0\}$$

we recover

$$\phi(\theta) = \frac{2+\theta}{3}. \tag{3.8}$$

Inserting Eq. (3.8) into the interface values Eq. (3.5) results in the quadratic reconstruction Eq. (3.1).

The total variation-control parameter $q$ can, in the TVD-MUSCL framework, also be interpreted as a control value of compressivness, similar to the minmod and super-bee limiter. Indeed, the smaller the parameter $q$, the more local variation is introduced in LDLR, resulting in spurious oscillations. In other words the function $\phi(\theta)$ moves out of the TVD region (see Fig. 2, right). The larger the $q$ the less the variation is produced and discontinuities are smeared out within more cells. This is similar to the transition between the diffusive minmod limiter and the over-compressive super-bee limiter inside Harten's TVD bound. Though for both limiters, minmod and super-bee, variation diminishes in the presence of discontinuity. The non-linear limiter function smoothly extends into the range of $\theta < 0$ and vanishes for $\theta \to \pm\infty$ and $\theta \to 0$, which is essential for limiting discontinuities.

Note that the derivation of the new limiter function Eqs. (3.6) and (3.7) and the limiter itself are essentially different from known limiters and their derivation (see Waterson and Deconinck [34] for a review). Here we have taken a new and successful approach, which features a non-linear and non-polynomial Ansatz function for the reconstruction, and have reduced it to a limiter function. The new limiter is simpler and more efficient than the original LDLR reconstruction and seems to go beyond the limiter categories described in [34].

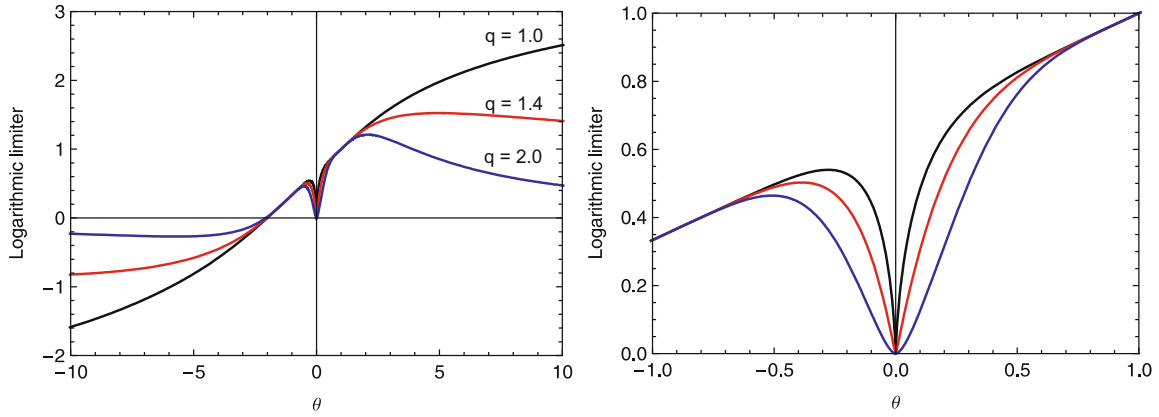


**Fig. 1.** Shape of the limiter function $\phi(\theta)$ Eq. (3.6) for different values of q. For larger $q$ less total variation appears, yet diffusion increases leading to smeared discontinuities. Right: Zoom of the inner region.

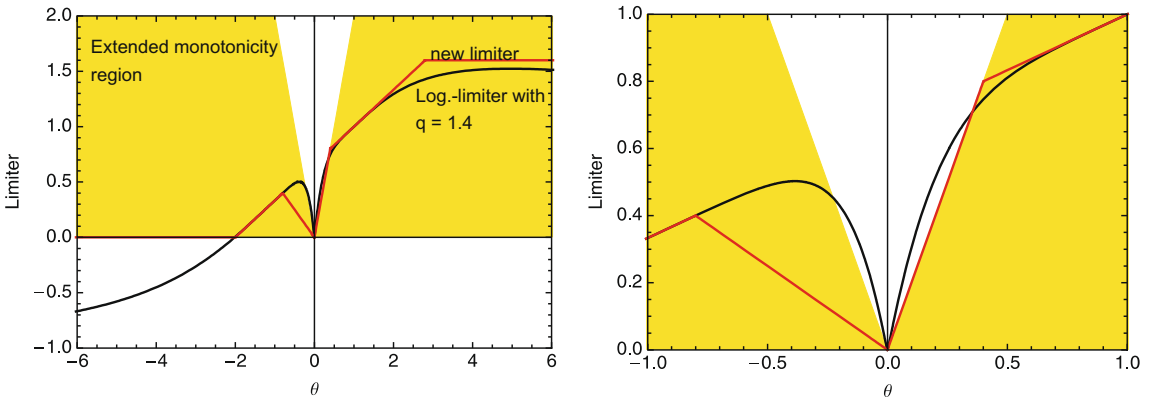


**Fig. 2.** Left: New limiter $\hat{\phi}$ Eq. (3.13) matching for logarithmic limiter with $q = 1.4$. Right: Zoom of the inner region. Extended monotonicity region according to [10].

### 3.3. Simplified third-order limiter

The logarithmic limiter $\hat{\phi}(\theta)$ is derived from a double logarithmic Ansatz function, which is conservative, third-order accurate and essentially local variation bounded. The essential characteristics are:

(1) $\phi(1+\Delta x) = 1 + \frac{\Delta x}{3} + \mathcal{O}(\Delta x^m)$ and $\phi(-1+\Delta x) = \frac{1}{3} + \frac{\Delta x}{3} + \mathcal{O}(\Delta x^n)$ with $n, m \geqslant 2$.
(2) $\lim_{\theta\to 0}\phi(\theta) \to 0$ and $\lim_{\theta\to\pm\infty}\phi(\theta) \to 0$.

The first condition guaranties a third-order accurate resolution of local extrema, for which $\theta = \pm 1 + \Delta x$ holds. The second ensures Eq. (3.6) to be local variation bounded in the presence of discontinuities.

Both, the LDLR and the logarithmic limiter function are eventually complicated and computationally expensive, although Eq. (3.6) has already only one logarithmic evaluation. Furthermore the LDLR is very sensitive to the parameter $q$ and Artebrant and Schroll [5] suggested to set $q = 1.4$ to ensure stability (see discussion above). Keeping the main features (1) and (2) in mind, we can construct a piecewise-linear limiter function with similar properties, yet even improving its shock capturing abilities.

Omitting logarithmic functions, we not only avoid troublesome singularities but also get better control on the reconstruction routine, thus on the total variation. The new limiter reads:

$$\hat{\phi}(\theta) = \max\left[0, \min\left(\frac{2+\theta}{3}, \max\left[-\alpha\theta, \min\left(\beta\theta, \frac{2+\theta}{3}, \gamma\right)\right]\right)\right], \tag{3.9}$$

where the parameters $\alpha, \beta$ and $\gamma$ satisfy the conditions:

$$\begin{cases} 0 \leqslant \alpha \leqslant 2, \\ 1 \leqslant \beta \leqslant 2, \\ 1 \leqslant \gamma \leqslant 2. \end{cases} \tag{3.10}$$

These parameters control the shock capturing properties and total variation of the limiter $\hat{\phi}(\theta)$, similar to the exponent $q$ in Eq. (3.7). They span a monotonicity region for the slope $\hat{\phi}(\theta_i)\delta_{i+1/2}$, i.e a region where the resulting interpolated function (reconstructed cell interface value) is monotone if the data are monotone. The region in Fig. 2 is included in the extended monotonicity regions proposed by Huynh [10] and Hyman [11]. Other authors, such as Spekreijse [25] and Dubois [6] (and references there in) have derived further constraints on the monotonicity region, bounding the parameter $\alpha$ by $0 \leqslant \alpha \leqslant 2 - \gamma$. This restriction reduces the region of full third-order recovery, but also restricts the maximum bound of total variation. This eventually leads to smeared discontinuities. We have to clearly emphasize that the monotonicity bounds derived by Spekreijse [25] are based upon symmetry assumptions for second-order reconstructions. Since we consider third-order reconstruction we impose different symmetry requirements Eq. (3.12) for the limiter function $\hat{\phi}(\theta)$. This leads to more relaxed monotonicity bounds for the limiter function: $\hat{\phi}(\theta) \in [-3\min(1,|\theta|), 3\min(1,|\theta|)]$ (see [10,11]). However monotonicity restrictions require that the slope $\hat{\phi}(\theta_i)\delta_{i+1/2} = 0$ if the data are not locally monotone, i.e., in the presence of local extrema and discontinuities. Therefore TVB methods, such as LDLR or ENO/WENO schemes relax the monotonicity conditions, in order to resolve smooth extrema to full accuracy.

The building block of the new limiter is the function $\phi(\theta) = \frac{2+\theta}{3}$ from Eq. (3.8), which results in the quadratic reconstruction Eq. (3.1). The variables $\alpha$ and $\beta$ bound the variation of $\hat{\phi}(\theta)$ for $\theta \in (-\infty, 0]$ and $\theta \in [0, 1]$, respectively. The parameter $\gamma$ represents the upper bound for the third-order reconstruction for $\theta \in [1, +\infty)$. We bound the variables $\beta$ and $\gamma$ according to the TVD region Eq. (2.9), to satisfy Harten's TVD theorem. So if we set $\alpha = 0$ we recover a TVD limiter

$$\phi^{\mathrm{TVD}}(\theta) = \max\left[0, \min\left(2\theta, \frac{2+\theta}{3}, 2\right)\right], \tag{3.11}$$

which essentially reconstructs smooth functions, for which $\theta \in \left[\frac{2}{5}, 4\right]$, to third-order accuracy. Still degenerating to first order for smooth extrema in $\theta \leqslant 0$. This function obviously is very economic and simple. Its evaluation only consists of two $(\max, \min)$ statements identical to the minmod limiter, yet it employs a quadratic polynomial reconstruction as building block. This limiter is essentially identical to the $\kappa = \frac{1}{3}$ Koren limiter [13]. It was originally derived from the $\kappa$-scheme of Anderson, Thomas and van Leer [2]. Koren used in his formulation the inverse $r = \frac{\delta_{i+1/2}}{\delta_{i-1/2}}$ of the slope ratio $\theta$ as smoothness measure. Therefore the cell interface values $\hat{u}^{(\mp)}_{i\pm\frac{1}{2}}$ Eq. (3.5) have to be reformulated under the consideration of $\phi^{\mathrm{TVD}}(\theta)\delta_{i+1/2} = \psi^{\mathrm{Koren}}(r)\delta_{i-1/2}$. In the following we will refer to the limiter $\phi^{\mathrm{TVD}}(\theta)$ Eq. (3.11) as Koren limiter to emphasize its original derivation. A similar limiter function has also been proposed by Arora and Roe [3] in the context of one-step FV methods. Although they employed a quadratic reconstruction for $\theta \approx 1$, the one-step algorithm is only second-order accurate for non-linear equations. Similar to classical second-order TVD limiters the Koren limiter (or $\phi^{\mathrm{TVD}}(\theta)$) and the Arora limiter [3] suffer from the clipping of extrema for $\theta \leqslant 0$ and do not recover the full order of accuracy.

To be able to capture smooth extrema for $\theta \approx -1$ without loss of accuracy, we have to ease the monotonicity requirement, i.e., Harten's TVD theorem. Setting $\alpha \geqslant \frac{1}{3}$ expands the limiter function continuously for $\theta \approx -1$ and allows to recover smooth extrema for $\theta \in \left[-2, -\frac{2}{3\alpha+1}\right]$ to a third-order accuracy.

A further attribute of the proposed limiter is that it does not satisfy the symmetry requirement of classical second-order TVD limiters

$$\phi(\theta^{-1}) = \phi(\theta)\theta^{-1} \quad \forall\theta \in \mathbb{R} \setminus \{0\}.$$

Suppose the data $\bar{u}^n$ are symmetric in $x$, we want to impose symmetry on the reconstruction, i.e., $\hat{u}^{(+)}_{i+\frac{1}{2}} = \hat{u}^{(-)}_{i+\frac{3}{2}}$. This requires that the limiter function $\hat{\phi}(\theta)$ satisfies

$$\begin{cases} 1 \leqslant \hat{\phi}(\theta) \leqslant \theta\hat{\phi}(\theta^{-1}) \leqslant \theta, & \theta \in [1, \infty), \\ \theta \leqslant \theta\hat{\phi}(\theta^{-1}) \leqslant \hat{\phi}(\theta) \leqslant 1, & \theta \in (-\infty, 1] \setminus \{0\}, \end{cases} \tag{3.12}$$

which is due to the inverse evaluation of $\theta$ in Eq. (3.5).

In Fig. 2 we match the new limiter $\hat{\phi}(\theta)$ with the original logarithmic limiter function $\phi(\theta, q = 1.4)$, Eqs. (3.6) and (3.7). The new limiter reads

$$\hat{\phi}(\theta) = \max\left[0, \min\left(\frac{2+\theta}{3}, \max\left[-0.5\theta, \min\left(2\theta, \frac{2+\theta}{3}, 1.6\right)\right]\right)\right]. \tag{3.13}$$

It shares the common characteristics of the logarithmic limiter within the simple framework of classical second-order TVD limiters. It is a piecewise-linear $(\max, \min)$ function which acts as a logical switch depending on the smoothness measure $\theta$. Its rigorous cutoffs for $\theta \to \pm 0$ (Fig. 2, right) ensure sharp resolution of discontinuous functions, yet remaining in Harten's TVD region for $\theta \geqslant 0$. Note that with $\alpha > 2 - \gamma$ we have violated Dubois [6] monotonicity conditions.

### 3.4. Geometrical interpretation of the TVD conditions

In the previous section we have derived a new limiter $\hat{\phi}(\theta)$, which reconstructs smooth extrema, for which $\theta \approx \pm 1$ holds, with a quadratic polynomial. Unfortunately in this form, the accuracy of the reconstruction still degenerates to first-order in cells with one vanishing lateral derivative. In the following we will discuss the problem of resolving smooth extrema for which $\theta \approx \pm 0$ holds with the aid of limiters.

Let us now consider a non-monotone sinusoidal initial function localized at different time levels on an equidistant grid. Fig. 3 illustrates the smooth profile as well as the discrete set of cell mean values $\{\bar{u}_{i-1}, \bar{u}_i, \bar{u}_{i+1}\}$, i.e., its discrete representation. The reconstruction of the interface values, based upon the three cells is shown at three different times. It is obvious that for the times $t_2$ and $t_3$, the slope ratio becomes $\theta \leqslant 0$. Thus limiters satisfying Harten's TVD constrains recover only the cell mean value itself and consequently clip-off local extrema. For $t_1$, where the data $\bar{u}_i$ are monotone in the interval $[x_{i-1}, x_i, x_{i+1}]$, $\theta \approx 1$ holds and full reconstruction is assured. Using the limiter $\phi^{\mathrm{TVD}}(\theta)$ improves the accuracy of the reconstruction only where the data $\bar{u}_i$ are monotone using a quadratic instead of a linear polynomial.

Since our reconstruction entirely depends on the lateral derivatives, we expand $\delta_{i\pm1/2}$ around $x_{i-1/2}$:

$$\begin{aligned} \delta_{i-1/2} &= u'(x_{i-1/2})\Delta x + \frac{1}{12}u'''(x_{i-1/2})\Delta x^3 + \mathcal{O}(\Delta x^4), \\ \delta_{i+1/2} &= u'(x_{i-1/2})\Delta x + u''(x_{i-1/2})\Delta x^2 + \frac{7}{12}u'''(x_{i-1/2})\Delta x^3 + \mathcal{O}(\Delta x^4). \end{aligned} \tag{3.14}$$

It is obvious that the lateral differences are given by

$$\delta_{i-1/2} = \delta_{i+1/2} + c_0\mathcal{O}(\Delta x^2) \quad \text{with } c_0 = u''(x_{i\mp1/2}) \tag{3.15}$$

for monotone data. For smooth data the lateral differences are bounded functions $\delta_{i\pm1/2} = \mathcal{O}(\Delta x)$, thus the local smoothness measure Eq. (2.8) yields

$$\theta = 1 - c_1 \mathcal{O}(\Delta x) \quad \text{with } c_1 = \frac{u''(x_{i\mp 1/2})}{u'(x_{i\mp 1/2})}. \tag{3.16}$$

Due to condition (1) in Section 3.3 we then reconstruct the interface values to full third-order accuracy, i.e., $\lim_{\Delta x \to 0}\theta = \pm 1$. For $\delta_{i-1/2} \approx 0$ and $\delta_{i+1/2} = c$ (or vice versa), one of the approximations of the lateral derivatives is an unbounded function with a singularity in the gradient at $\Delta x \to 0$. Then the data are discontinuous and we have to limit the reconstruction completely, i.e., either $\lim_{\Delta x \to 0}\theta = \pm\infty$ or $\lim_{\Delta x \to 0}\theta = \pm 0$.

In order to achieve full third-order accuracy for monotone data, the constant $c_1 = \frac{u''(x_{i\mp 1/2})}{u'(x_{i\mp 1/2})}$ must be a bounded function. Yet it is also obvious that on a coarse grid this constant might change the convergence order dependent on the curvature of the data. The constant $c_1$ represents a measure of curvature for a monotone function between two neighboring cells. For a rather large $|c_1|$, i.e., $|u'|$ small and/or $|u''|$ large, the discretized input data, especially on a coarse grid, might represent a discontinuity rather than a smooth function. Consequently such data will be fully limited. Note that in the vicinity of steep, narrow extrema $|c_1|$ will also be very large yet still bounded ($|u'| \neq 0$) and a fine resolution is needed to accurately reconstruct the function with only three data points.

The characteristic of a limiter to reconstruct linear functions with a large constant $|c_1|$ is often referred to as compressivness. It is controlled by the limits of Harten's TVD conditions Eq. (2.9), especially by the lower bound $\phi(\theta) \leqslant \beta\theta$ with $1 \leqslant \beta \leqslant 2$ (see Eq. (3.10)). Choosing a smaller limit $\phi(\theta) = \theta$ yields a more diffusive limiter, such as the minmod function. Increasing the bound to $\phi(\theta) \leqslant 2.5\theta$, the limiter is outside Harten's TVD region, but it reconstructs steeper transitions, i.e., linear function with a "larger" constant $|c_1|$, to full third-order accuracy. This is the case for the logarithmic limiter Eq. (3.6) of the LDLR reconstruction as can be seen clearly in Fig. 2 (right picture). But it also leads to spurious over-and under-shoots, since the limiter is outside Harten's TVD bounds. This is the reason why we choose the lower limit to be inside the TVD region. If the constant $|c_1|$ is small, for shallow gradients, we have $\theta = 1 + \mathcal{O}(\Delta x)$ and we yield third-order recovery.

To be able to recover smooth extrema with different signs of the lateral derivatives, i.e., $\theta = -1$, the monotonicity condition has to be softened. The extended monotonicity region, Fig. 2, is indicating a domain where the resulting interpolated function, i.e., the reconstructed values are monotone, even though the data are not necessarily monotone (Fig. 3 for $t_3$). Although we have already extended here the limiter $\hat{\phi}(\theta)$ for $\theta < 0$, we can only fully reconstruct local extrema that are almost perfectly symmetric at the cell center $x_i$ and therefore its slopes $\delta_{i\pm 1/2}$ are of same absolute value but are of different signs ($\theta \approx -1$). As shown in Fig. 3 this is a very artificial case, since local extrema although initially located at a cell center, will eventually be relocated during their evolution inside the cell.

It is crucial to understand, that although the LDLR algorithm is of third-order accuracy, the derived logarithmic limiter Eq. (3.6) and also its simplification Eq. (3.9) suffers from accuracy loss at local extrema for which $\theta \to 0$ or $\theta \to \pm\infty$. Hence smooth extrema with one vanishing lateral derivative are always limited instead of being fully reconstructed. Fig. 3, for $t_2$.

In order to overcome this drawback we have to extend the new limiter formulation. We cannot just simply extend the monotonicity region in Fig. 2, so long $\hat{\phi}(0) = 0$ holds. We have to formulate a criterion that prohibits the limiter $\hat{\phi}(\theta)$ to pass through zero in the presence of a local extremum with one vanishing lateral derivative. For this we have introduced an asymptotic region based on the indicator function

$$\eta(\delta_{i-1/2}, \delta_{i+1/2}) = \frac{\delta_{i-1/2}^2 + \delta_{i+1/2}^2}{(r\Delta x)^2}, \tag{3.17}$$

which is a function of the lateral differences $\delta_{i\pm 1/2}$, instead of $\theta$. In addition it depends on the grid size $\Delta x$ and on a dimensionless constant $r > 0$. We will refer to the constant $r$ as radius of the asymptotic region.

For $\eta \leqslant 1$ the lateral derivatives $\delta_{i\pm 1/2}$ are too small for $\theta$ being a good measure for discontinuities. For $\eta > 1, \delta_{i\pm 1/2}$ are large enough so that the limiter $\hat{\phi}(\theta)$ can be applied. In Fig. 4 one can see that the asymptotic region spans a circle around

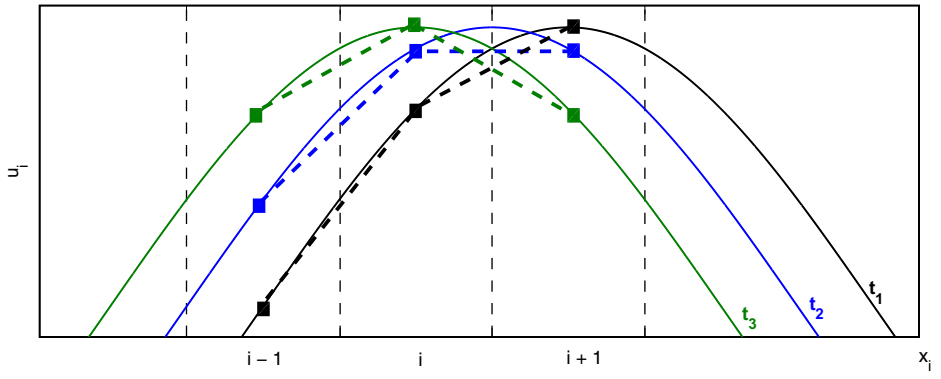


**Fig. 3.** Sketch of a smooth initial profile and its discrete representation at different times, i.e., different locations on a uniform grid. For simplicity we have drawn point values instead of cell mean values.

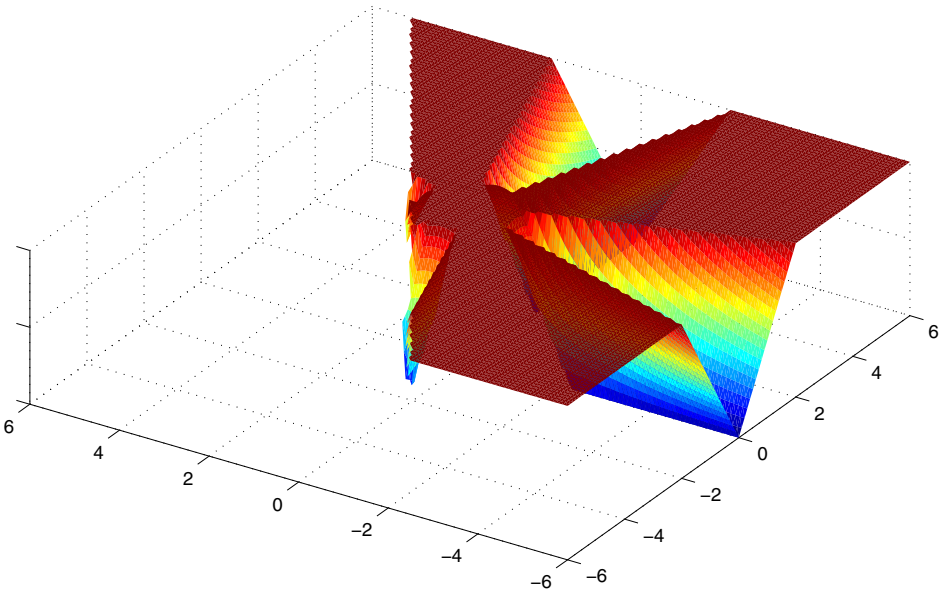


$\theta \approx \pm 0$ with the radius $r$. Thus data inside this domain are reconstructed to full third-order accuracy, whereas data outside the asymptotic region are passed to the limiter $\hat{\phi}(\theta)$ Eq. (3.9).

Assuming a local extremum $u'(x_{i-1/2}) = 0, u''(x_{i-1/2}) \neq 0$ and canceling higher-order terms in Eq. (3.14), Eq. (3.17) yields

$$\eta(\delta_{i-1/2}, \delta_{i+1/2}) = \left(\frac{u''(x_{i-1/2})}{r}\right)^2 \Delta x^2 + \mathcal{O}(\Delta x^3). \tag{3.18}$$

The function $\eta$ is a measure of the second derivative, i.e., of the curvature of non-monotone data inside a cell. Note that $\eta = \mathcal{O}(\Delta x^2)$ which is smaller than the required linear convergence of $\theta$ Eq. (3.16) for a third-order reconstruction. In this perspective the quadratic convergence is optimal, since one cannot expect more from a three-point stencil.

Considering the case of smooth extrema with one vanishing lateral derivative in the discrete FV setting, i.e., $\delta_{i-1/2} = 0$ and $\delta_{i+1/2} = c\mathcal{O}(\Delta x^\tau)$. The asymptotic region $\eta$ becomes

$$\eta(0, c\mathcal{O}(\Delta x^\tau)) = \left(\frac{c}{r}\right)^2 \mathcal{O}(\Delta x^{2(\tau-1)}). \tag{3.19}$$

For data with a local extremum $\tau = 2$ and $c = u''(x_{i-1/2})$ and $\eta$ becomes

$$\eta(0, u''(x_{i-1/2})\mathcal{O}(\Delta x^2)) = \left(\frac{u''(x_{i-1/2})}{r}\right)^2 \mathcal{O}(\Delta x^2). \tag{3.20}$$

Consequently we are inside the asymptotic region, i.e., third-order reconstruction. For $\tau = 0$, one of the lateral slopes is constant yielding

$$\eta(0, c) = \left(\frac{c}{r}\right)^2 \mathcal{O}(\Delta x^{-2}), \tag{3.21}$$

hence second-order convergence towards infinity. Thus switching to the limiter $\hat{\phi}(\theta)$ already on a coarse grid in the presence of a jump discontinuity. It is significantly faster than the convergence order of total variation for LDLR $\mathcal{O}(\Delta x^{1.4} |\ln(\Delta x)|)$ [5] and $\mathcal{O}(\sqrt{\Delta x})$ for Marquina's hyperbolic reconstruction [18]. This is the reason why Marquina has still to preprocess the lateral derivatives to avoid spurious oscillation in the presence of jump discontinuities.

Once again it is important to consider the constants in the convergence analysis. In this case especially the ration $\frac{c}{r}$. In the presence of a local extremum at the cell interfaces the second derivative $c = u''(x_{i-1/2})$ represents a measure for the steepness of the data, i.e., for its curvature. The radius of the asymptotic region can account for large curvatures on coarse grids. This eventually leads to a faster – in term of mesh resolution $\Delta x$ – convergence of $\eta$ towards zero, i.e., to third-order accurate reconstruction. In the presence of discontinuities the constant $|c|$ simply represents the jump between two neighboring cells. For strong shocks $|c|$ will be large. With a small radius $0 < r \ll 1$ the asymptotic region $\eta$ converges faster towards infinity. It is important to understand that playing with the parameter $r$, i.e., increasing or decreasing the size of the asymptotic domain clearly affects the amount of introduced variation. Yet the function $\eta$ only affects region with one vanishing lateral derivative.

Finally our new third-order limiter function reads:

$$\phi^{\mathcal{O}(3)}(\delta_{i-1/2},\delta_{i+1/2}) = \begin{cases} \frac{2+\theta}{3} & \text{if } \eta \leqslant 1-\epsilon, \\ \hat{\phi}(\theta) & \text{if } \eta \geqslant 1+\epsilon, \\ \frac{1}{2}\left(\left(1-\frac{\eta-1}{\epsilon}\right)\frac{2+\theta}{3}+\left(1+\frac{\eta-1}{\epsilon}\right)\hat{\phi}(\theta)\right) & \text{else} \end{cases} \tag{3.22}$$

with $\epsilon$ being a small positive number, which is about the size of the particular machine precision and ensures Lipschitz continuity for $\phi^{\mathcal{O}(3)}$. Note that in the proposed limiter, the problem of accurately recovering smooth extrema with one vanishing lateral derivative and simultaneously reconstructing sharp gradients is rigorously decoupled. Consequently, in the presence of a discontinuity the new limiter yields $\phi^{\mathcal{O}(3)} \to \hat{\phi}(0) = 0$ with $\mathcal{O}(\Delta x^2)$ Eq. (3.21). This convergence rate towards zero total variation is significantly higher than that of Artebrant and Schroll's double logarithmic reconstruction or Marquina's hyperbolic reconstruction.

Fig. 4 points out the characteristic properties of the final limiter Eq. (3.22). It is, for simplicity, more a sketch rather than an actual plot of the function $\phi^{\mathcal{O}(3)}$. This way we can geometrically clarify the asymptotic region $\eta$, a confidence region and a transition domain. In the first two regions the interface values are reconstructed to full third order, since we are "confident" that the input data are smooth, i.e., $\tau = 2$ Eq. (3.20). Whereas in the transition region the discretized input data are discontinuous. In other words $\tau = 0$ Eq. (3.21) and consequently the data have to be fully limited. The lower limit $(1-\epsilon)$ and upper limit $(1+\epsilon)$, i.e. the thickness of the dark circle around the asymptotic region ensure Lipschitz continuity of $\phi^{\mathcal{O}(3)}$ and so for the numerical flux function $\mathcal{F}$ in Eq. (2.2) away from the asymptotic domain cuts along constant $\delta_{i-1/2}$ correspond to the limiter function, Fig. 2.

We want to emphasize that in this formulation the asymptotic region only affects smooth functions with one vanishing lateral derivative and is completely decoupled from the shock capturing limiter $\hat{\phi}(\theta)$. Once $\eta > 1+\epsilon$ the function $\hat{\phi}(\theta)$ is switched on. This limiter, as discussed before, satisfies at least for $\theta > 0$ Harten's TVD constraints, thus not producing variation at all. Note that numerical experiments indicate, that the region for $\theta < 0$ is very seldom evaluated, namely when the smooth extremum is precisely located at the cell center. Most of the time the cells for which $\theta \approx \pm 1$ holds are affected. From the reconstruction point of view, this means that these cells have to be identified as fast as possible, when refining cell size $\Delta x$. Therefore the choice of the radius $r$ is crucial. This variable, at least on a coarse grid, controls the compressivness of $\eta$ Eqs. (3.20) and (3.20), respectively. This is critical since discretized shallow gradient or smooth extrema eventually have identical curvature for a certain grid size $\Delta x$. Because of this we recommend, especially for intermediate jump discontinuities on coarse grids, to set $r \in [0.001, 1]$. We prefer to produce as small variation as possible. Numerical experiments, however, indicate that $r > 1$ is possible and in certain examples significantly improves the accuracy (see Fig. 17). Eventually the asymptotic region always converges quadratically to the correct limit faster than LDLR. This compromise is the ultimate, independent of the reconstruction Ansatz function, for a local three-point stencil.

## 4. Time integration

Since numerical errors in time and space discretization can be swapped, we need to adjust the time-marching scheme. Third-order accuracy in time is accomplished by integrating the finite volume update Eq. (2.2) using the explicit third-order TVD Runge–Kutta method of Gottlieb and Shu [7].

This specific Runge–Kutta scheme consists of a single Euler's step repeated thrice

$$\boldsymbol{u}^{n+1} = \boldsymbol{u}^n + \Delta t \boldsymbol{L}\boldsymbol{u}^n = \boldsymbol{M}(\Delta t \boldsymbol{L})\boldsymbol{u}^n. \tag{4.1}$$

This is a system of explicit linear equations with the matrix operator $\boldsymbol{L}$ containing the non-linear spatial approximation for the discrete set of values $\boldsymbol{u}^{n+1} \equiv \{u_i^{n+1}, n = \ldots 0, 1, 2, \ldots\}$, i.e., $\boldsymbol{L}\boldsymbol{u}^n = L_i(u^n)$.

For the explicit Euler time-marching scheme the operator $\boldsymbol{M}$ reads

$$\boldsymbol{M}(\Delta t \boldsymbol{L}) = \boldsymbol{I} + \Delta t \boldsymbol{L}, \tag{4.2}$$

and for the explicit thee-stage Runge–Kutta method

$$\boldsymbol{M}(\Delta t \boldsymbol{L}) = \boldsymbol{I} + \Delta t \boldsymbol{L} + \frac{1}{2}(\Delta t \boldsymbol{L})^2 + \frac{1}{6}(\Delta t \boldsymbol{L})^3. \tag{4.3}$$

Note $\boldsymbol{M}$ is a polynomial in the spatial operator $\Delta t \boldsymbol{L}$.

To investigate the linear stability of the algorithm we assume $\boldsymbol{L}$ to be linear. We consider the time evolution of a sinusoidal grid function in an unbounded domain, with $a > 0$ governed by the scalar linear advection equation

$$u_t + a u_x = 0, \quad u_k(x,0) = v_k(0) e^{\boldsymbol{i}kx}, \quad x \in (-\infty, \infty), \tag{4.4}$$

where $v_k(t)$ is the Fourier transform of the exact solution, $k = 2\pi/\lambda$ is the wave number and $\boldsymbol{i}$ represents the imaginary unit. Discretizing Eq. (4.4) on a grid with uniform spacing $\Delta x$ we can calculate the complex amplitude, i.e the amplification factor of a numerical scheme

$$\frac{v_k^{n+1}}{v_k^n} = \boldsymbol{M}(\Delta t \widehat{L}(k)) \equiv z(k), \tag{4.5}$$

where $\widehat{L}(k) = \lambda_k$ are the eigenvalues of the spatial operator $\boldsymbol{L}$. This amplification factor is an approximation of the amplification factor of the exact advection equation (4.4):

$$z^{ex}(k) = \frac{u_k(x, \Delta t)}{u_k(x, 0)} = e^{-\boldsymbol{i}\nu k\Delta x}, \tag{4.6}$$

with the CFL number

$$\nu = \frac{a\Delta t}{\Delta x}. \tag{4.7}$$

Numerical stability, in the von Neumann sense, implies that the absolute value of the amplification factor $z(k)$ should not exceed unity. Hence the characteristic equation for the explicit third-order Runge–Kutta method reads

$$|z(k)| = |1 + \Delta t\lambda(k) + \frac{1}{2}(\Delta t\lambda(k))^2 + \frac{1}{6}(\Delta t\lambda(k))^3| \leqslant 1. \tag{4.8}$$

Applying the quadratic reconstruction Eq. (3.1) to the advection equation, we yield the semi-discretization

$$\frac{d}{dt}u_i = -a\left(\frac{3u_i + u_{i-2} - 6u_{i-1} + 2u_{i+1}}{6\Delta x}\right), \tag{4.9}$$

which corresponds to the complex spectrum

$$\Delta t\lambda_k = -\frac{1}{6}\nu e^{-\boldsymbol{i}k\Delta x}(e^{\boldsymbol{i}k\Delta x} - 1)(5 + \cos(k\Delta x) + 3\boldsymbol{i}\sin(k\Delta x)). \tag{4.10}$$

Inserting Eq. (4.10) into the characteristic equation of the explicit third-order Runge–Kutta method Eq. (4.8) yields the amplification factor of the Fourier mode. To obtain the amplification factor for the above scheme Eq. (4.9) with a second-order time-marching method, we have to drop $\mathcal{O}((\Delta t\lambda(k))^3)$ in Eq. (4.8).

Fig. 5 shows the absolute value of the amplification factor plotted against the reduced wave number $\tilde{k} = k\Delta x$ for different CFL numbers $\nu$. The left figure represents an explicit second-order time integration and the right one represents the three-stage Runge–Kutta time-marching scheme for Eq. (4.4). Both plots indicate that the scheme Eq. (4.9) is less dissipative for very small Courant numbers $|\nu| \leqslant 0.1$. However using the third-order time integration, the dissipation of high frequency waves gets reduced with large Courant numbers $|\nu| \geqslant 1.0$. Furthermore the third-order time-marching scheme, in contrast to the second-order one, gets unstable for high-frequency waves, but remains stable for small frequencies. The Fourier modes in the solution have in general the largest amplitude at low wave numbers.

From the numerical evaluation of the wave spectrum, we conclude that the explicit three-stage TVD Runge–Kutta method is stable for all values of the Courant number $|\nu| \lesssim 1.63$. Note that using only a second-order time-marching scheme plus the third-order spatial reconstruction we would obtain a more restrictive CFL condition $|\nu| \lesssim 0.83$.

Using a classical truncation error analysis in the frequency domain, we can recover the formal order of accuracy of the scheme. We consider the ratio of the numerical amplification factor and the exact one:

$$\mathcal{R}(\tilde{k}) = \frac{z(\tilde{k})^{nu}}{z(\tilde{k})^{ex}}. \tag{4.11}$$

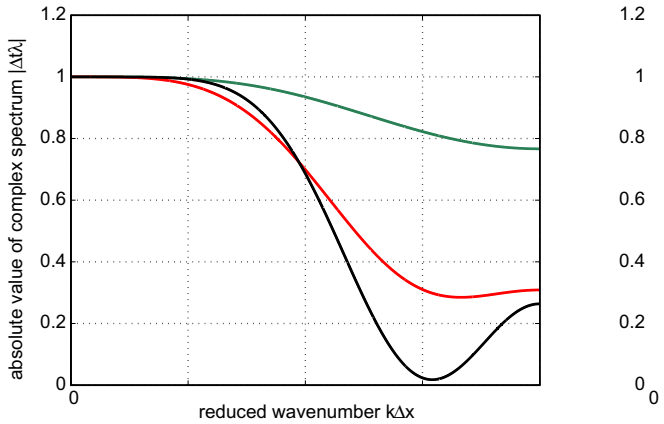

With a standard Taylor expansion we get for the third-order method Eq. (4.9) combined with a three-stage TVD Runge–Kutta time integrator

$$\mathcal{R}(\tilde{k})^{\mathcal{O}(3)} - 1 = -\frac{1}{24} v(2 + v^3)\tilde{k}^4 + \mathcal{O}(\tilde{k}^5). \tag{4.12}$$

The ratio of the amplification factors for the third-order scheme $\mathcal{R}(\tilde{k})^{\mathcal{O}(3)}$ approximates 1 to fourth-order $\mathcal{O}(\tilde{k}^4)$. The leading term is a real number which is associated with a diffusive character of the method. Comparing this quantity with only a TVD second-order time-marching scheme and the quadratic reconstruction Eq. (4.9) we obtain

$$\mathcal{R}(\tilde{k})^{\mathcal{O}(2)} - 1 = -\frac{1}{6}\boldsymbol{i}v^3\tilde{k}^3 - \frac{1}{24} v(2 - 3v^3)\tilde{k}^4 + \mathcal{O}(\tilde{k}^5). \tag{4.13}$$

This scheme is formally only of second-order accuracy $\mathcal{O}(\tilde{k}^3)$ with a dispersive character.

In Fig. 6 we compare numerical results for the linear advection equation (4.9). Two different time integration schemes, namely the second-order Heun and the three-stage Runge–Kutta method, are used. The unlimited third-order algorithm produces only small, yet symmetric and local, over-and under-shoots. The oscillation decay in time, since diffusion is dominant. In contrast, the second-order scheme with third-order spatial accuracy is dispersive and the oscillations disperse as time proceeds and completely destroy the shape of the initial profile.

We are aware that the von Neumann analysis gives only a sufficient condition for stability for linear operators $\boldsymbol{L}$. Our reconstruction is based upon a non-linear limiter function. Its behavior in the frequency domain cannot be completely represented by a linear stability analysis. Yet the analysis indicates the benefits using a three-stage Runge–Kutta time integration together with third-order spatial reconstruction. We not only obtain a far less restrictive CFL condition than using a second-order time-marching scheme, we also improve its dissipative character especially for high frequency waves and its shape preserving properties. Moreover due to the local character of the oscillations, the non-linear limiter function will only be limiting few cells around a discontinuity. Whereas in the second-order, dispersive, algorithm the limiter has to be applied on all cells to stabilize the computation.

## 5. Numerical experiments

In this section we conduct a series of convergence and accuracy tests from one-dimensional linear advection equation to two-dimensional Euler equations including also a pseudo convergence test for the one-dimensional ideal MHD equations.

### 5.1. One-dimensional scalar equations

We solve the scalar linear advection equation

$$u_t = -u_x, \quad u(t = 0, x) = u_0(x), \tag{5.1}$$

with different initial conditions on a periodic domain $x \in [-1, 1]$.

#### 5.1.1. Convergence studies for a smooth initial profile

**Example 1.** We solve the advection equation (5.1) with the initial condition $u_0(x) = \sin(\pi x)$. The initial profile is advected until $t = 1$. We conduct numerical experiments for different radii $r$ of the asymptotic region Eq. (3.17), to clarify its expansion

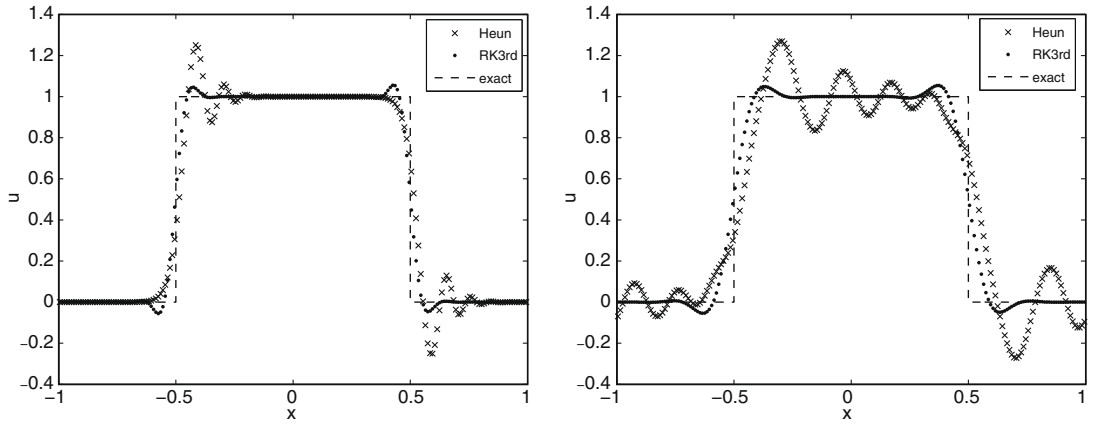


**Fig. 6.** Linear advection of a square wave: unlimited quadratic reconstruction with a second-order (×) and third-order (•) TVD time-marching scheme, until $t = 2$ (left) and $t = 20$ (right), $v = 0.8$ with 200 cells.

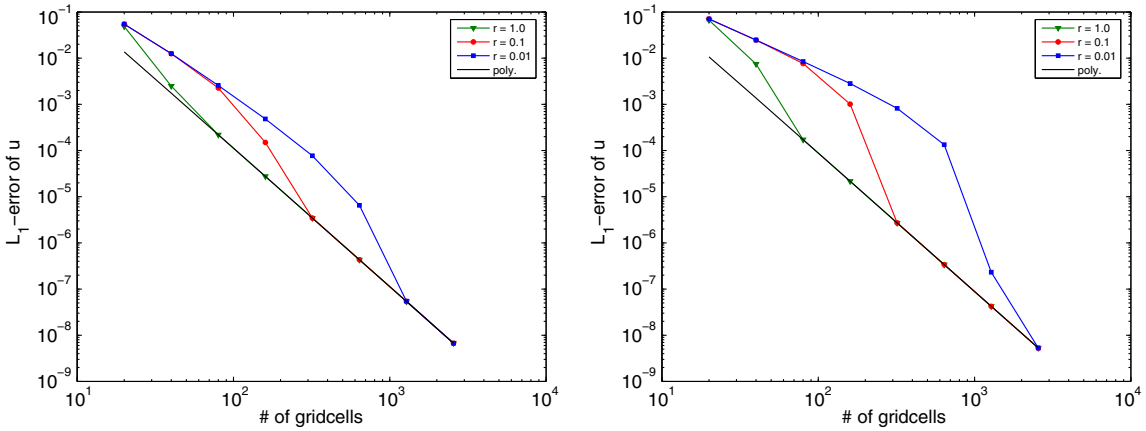


**Fig. 7.** Double-logarithmic plots of the error vs. number of grid cells for the advection equation with $u_0(x) = \sin(\pi x)$ at $t = 1$ with $v = 0.9$. Solution for different radii $r$ of the asymptotic region (3.17) are shown. Left: 1-norm errors, right: max-norm errors.

for the accuracy of the proposed scheme. Rather than presenting a table with the convergence rates calculated between two consecutive results, we have plotted in Fig. 7 the computed $L_1$- and $L_\infty$-errors obtained at $t = 1$ with Courant number $v = 0.9$. The discrete norms are given by:

$$\|e(\cdot,t^n)\|_{L_1} = \Delta x \sum_{i=1}^{N} |\bar{u}(x_i,t^n) - \bar{u}_i^n| \qquad \|e(\cdot,t^n)\|_{L_\infty} = \max_{1\leqslant i\leqslant N} |\bar{u}(x_i,t^n) - \bar{u}_i^n|. \tag{5.2}$$

Here $N$ is the number of computational cells. In this way we get a clear impression when – in terms of spatial resolution and radius $r$ – the designated error, i.e., the error of the unlimited quadratic polynomial reconstruction is reached. We have to keep in mind that no FV-reconstruction based on three cells can be more accurate than the pure quadratic polynomial reconstruction. Calculating the convergence rate between two consecutive results gives in all three cases, $r = 1.0, r = 0.1$ and $r = 0.01$, the formal third-order using only 40 cells. However it is obvious that the designated accuracy is only reached with more cells, especially for a small asymptotic region $r \leqslant 0.01$. Note that the curvature of our initial function is $|u''(x)| = \pi^2$. Whereas Artebrant and Schroll [5] use the initial function $u_0(x) = 1.0 + 0.2\sin(\pi x)$ with smaller curvature $|u''| = 0.2\pi^2$. Consequently they recover third-order convergence rate setting the variational-control parameter $q = 1.4$ (see Eqs. (3.6) and (3.7)) with 40 grid cells. Using the same initial data we recover the desired convergence error for $r = 1.0$ with only 10 cells, hence faster. This is due to the fact that $\eta = \mathcal{O}(\Delta x^2)$ for smooth extrema.

Fig. 8 shows two different solutions of the advection equation: one obtained with a step function and one with a sin wave as initial function $u_0(x)$. The picture clearly points out the effect of the asymptotic region for different radii $r$. Choosing a small radius $r \leqslant 0.01$, the limiter needs a sufficient resolution, around 200 cells, to be able to distinguish between a discretized smooth extremum or a shallow gradient. Note that the two profiles are advected ten times ($t = 20$) around the domain $x \in [-1, 1]$. We can also observe that even for a large asymptotic region, essentially no limiting, the method does not

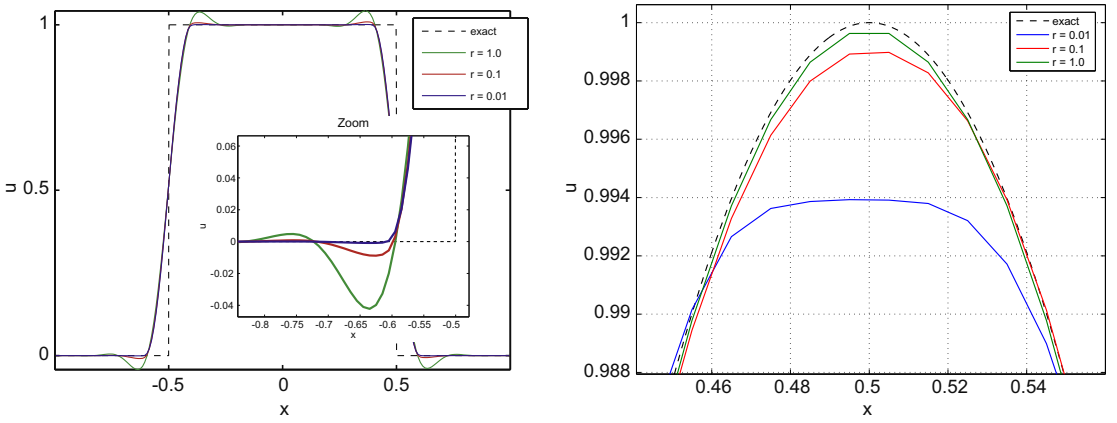


**Fig. 8.** Solution of the advection equation with a square wave (left) and a sin-wave (right) as initial conditions. Results are calculated at $t = 20$ with $v = 0.8$ using 200 cells for different expansion of the asymptotic region.

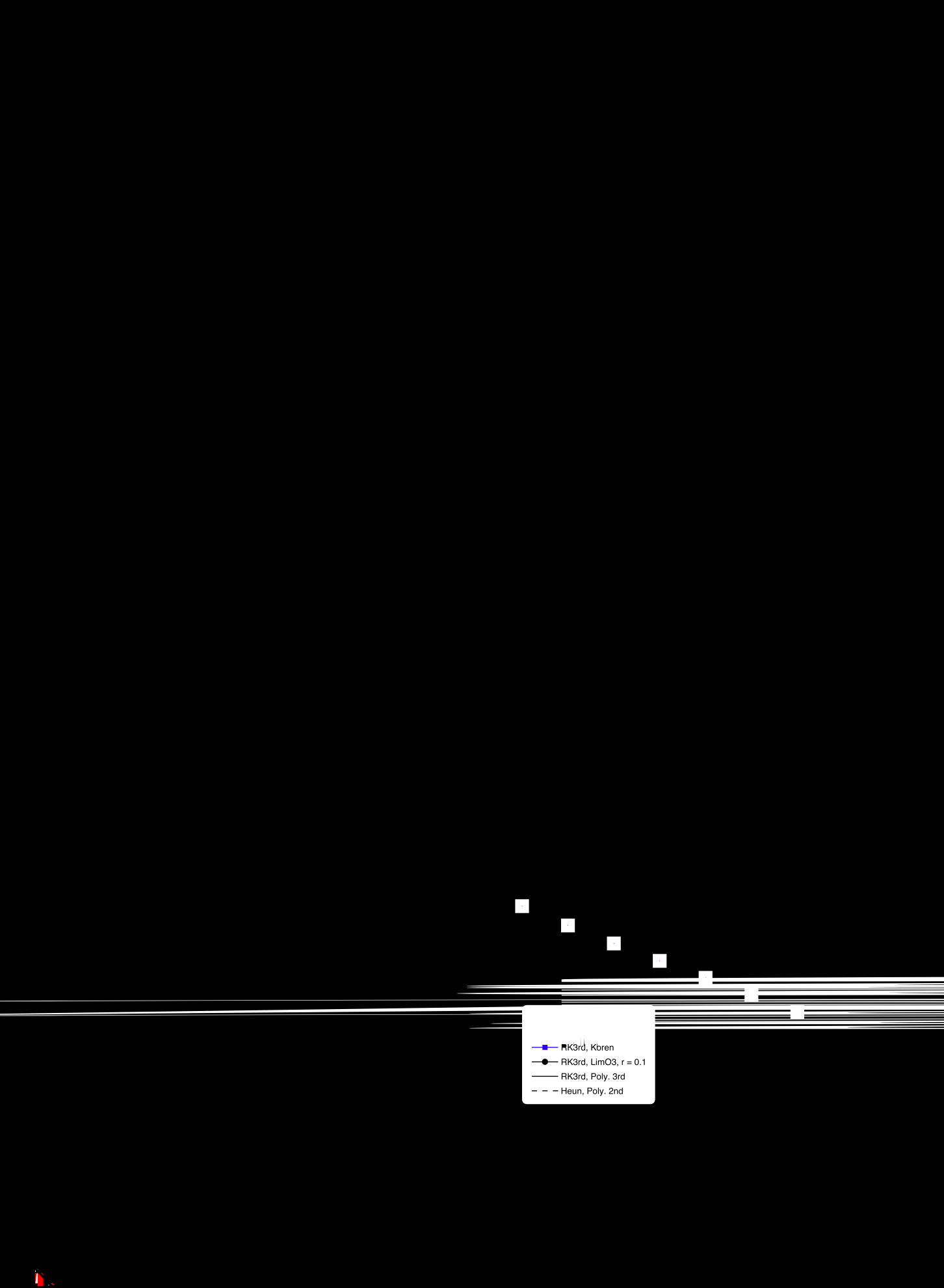
RK3rd, Kbren
RK3rd, LimO3, r = 0.1
RK3rd, Poly. 3rd
Heun, Poly. 2nd

$$\frac{\mathrm{d}\hat{\phi}}{\mathrm{d}\theta}(0^-) = -\frac{1}{2}. \tag{5.4}$$

Hence the limiter $\hat{\phi}(\theta)$ Eq. (3.13) uses also information for the reconstruction from the neighboring cells for $-2 \leqslant \theta < 0$.

Switching on the asymptotic region, hence using limiter $\phi^{\mathcal{O}(3)}$ Eq. (3.22) with radius $r = 0.1$ improves the convergence results significantly. The initial profile exhibits large curvatures $|u''| \approx 39.5$ at the vicinity of the two extrema. Therefore the full accuracy of the unlimited quadratic reconstruction in the max-norm is recovered not until about 1000 grid-cells resolution. Yet the use of the asymptotic region already improves the accuracy with less computational cells in both norms. Note that no accuracy degeneracy, as reported in [23] for third-order ENO schemes, was found with the proposed algorithm (RK3rd, LimO3, $r = 0.1$ with asymptotic region).

We can clearly observe that the unlimited second-order scheme (dashed line) needs about 6000 grid cells to achieve the same accuracy as the RK3rd, Koren-limiter method (or RK3rd LimO3, respectively), which cuts of smooth extrema. Consequently for this example modified second-order algorithms as proposed by Venkatakrishnan [33] or van Albada [30] will also need at least 6000 computational cells and introduce slight oscillations [33]. We did not observe any spurious oscillations, neither with RK3rd $\phi^{\mathrm{TVD}}(\theta)$ Eq. (3.11) nor with RK3rd $\hat{\phi}(\theta)$ Eq. (3.13).

Although the computational effort increases with the number of stages in the time integrator, it is difficult to achieve the accuracy of the third-order schemes (RK3rd, LimO3, $r = 0.1$ with asymptotic region) with second-order methods (see Fig. 9). The analysis of Section 4 suggests that we can use larger time steps with the new algorithm. This increases the computational efficiency, even in comparison to second-order methods, without loss of accuracy.

*5.1.2. Initial condition with discontinuities*

We take a test case, proposed in [12]. It consists of a tight combination of four waves, namely a smooth but narrow Gaussian peak, a square wave, a triangle wave and a half ellipse. The triangle has a smooth transition at its base. We use periodic boundary conditions on the domain $x \in [-1, 1]$ and the initial profile is advected until $t = 20$.

In Fig. 10 we compare our new limiter function $\phi^{\mathcal{O}(3)}$ (LimO3) with third-order ENO method (ENO3) and with Artebrant and Schroll's LDLR. ENO3 is essentially not local since it uses a five-point stencil to choose between the "smoothest" quadratic reconstruction for the interface values. All schemes use the same explicit third-order Runge–Kutta method for time integration. Since our method has a less restrictive CFL condition, we run the experiment with $\nu = 0.8$, instead of $\nu = 0.6$ for ENO3 and LDLR.

Especially in contrast to the classical TVD-MUSCL scheme (see e.g. [32]), the new method gives a good approximation of the exact profile. Typical drawbacks of second-order TVD limiter, such as smearing and squaring of linear waves are completely avoided. The results are perfectly symmetric and corners a very well resolved. The symmetry of the results is due to the fact, that near $\theta = 1$ we recover a smooth function of second degree and the formal third-order accuracy. Whereas second-order TVD limiters, such as super-bee or minmod, are only Lipschitz continuous near $\theta = 1$. This drawback enhances the probability, that the wrong choice of slopes is used for the one-sided approximation. However even smooth limiters, such as van Leer, MCD (see e.g. [15]) or van Albada [30] do not give symmetric profiles (see e.g. [32]). Furthermore we can observe that results obtained with the third-order limiter $\hat{\phi}(\theta)$ Eq. (3.9) using only a second-order time-marching scheme loose their symmetry completely (see Fig. 10, bottom profile). As already indicated in Section 4 and in the previous convergence studies, the formal order of the complete algorithm is essential not only for its accuracy, but also for its shape-preserving quality.

Both LimO3 and LDLR are essentially of the same quality, yet LimO3 has a higher Gaussian peak and produces less overshoots for the half ellipse. Whereas ENO3 is not able to distinguish between the different waves and always produces sinusoidal-like wave patterns. All three methods produce negative values, yet for LimO3 they are of a smaller magnitude. Remember the asymptotic region scales, in the presence of jump discontinuities, with $\mathcal{O}(\Delta x^{-2})$ Eq. (3.21).

In the bottom profile of Fig. 10 we can also observe the relevancy of the shape of the limiter for $\theta < 0$. We have used the limiter

$$\hat{\phi}(\theta) = \max\left[-1, \min\left(\frac{2+\theta}{3}, \max\left[-2\theta, \min\left(2\theta, \frac{2+\theta}{3}, 2\right)\right]\right)\right] \tag{5.5}$$

and compared it to $\phi^{\mathrm{TVD}}(\theta)$ Eq. (3.11). It is obvious that in this form the limiter violates the monotonicity region of [25] or [6], yet we still could not observe any over-or under-shoots. But in comparison to $\phi^{\mathrm{TVD}}(\theta)$ the amplitude of all four waves is better resolved. It is necessary to use Heun time integrator in order to emphasize these effects. The limiter $\hat{\phi}(\theta)$ Eq. (5.5) reconstructs cells for which $\theta \in \left[-5, -\frac{2}{7}\right]$ hold to full third-order accuracy. This results in a more accurate approximation of the wave peaks. Note that we have significantly stretched the region of third-order reconstruction for $\theta < 0$ in order to clearly demonstrate its effects. For further calculations we remain in the monotonicity region proposed by Spekreijse [25], and use the proposed limiter function in Section 3 Eq. (3.13).

A comparison of the Koren limiter Eq. (3.11) with LimO3 ($r = 0.01$) Eq. (3.22) employing RK3rd time integrator shows eventually no significant difference on the used grids. We have to either significantly refine the grid to see eventually a better resolved smooth half ellipse for $0.4 \leqslant x \leqslant 0.6$ or enlarge the asymptotic region, yet introducing more local variation. The effects are depicted in detail in Fig. 8.

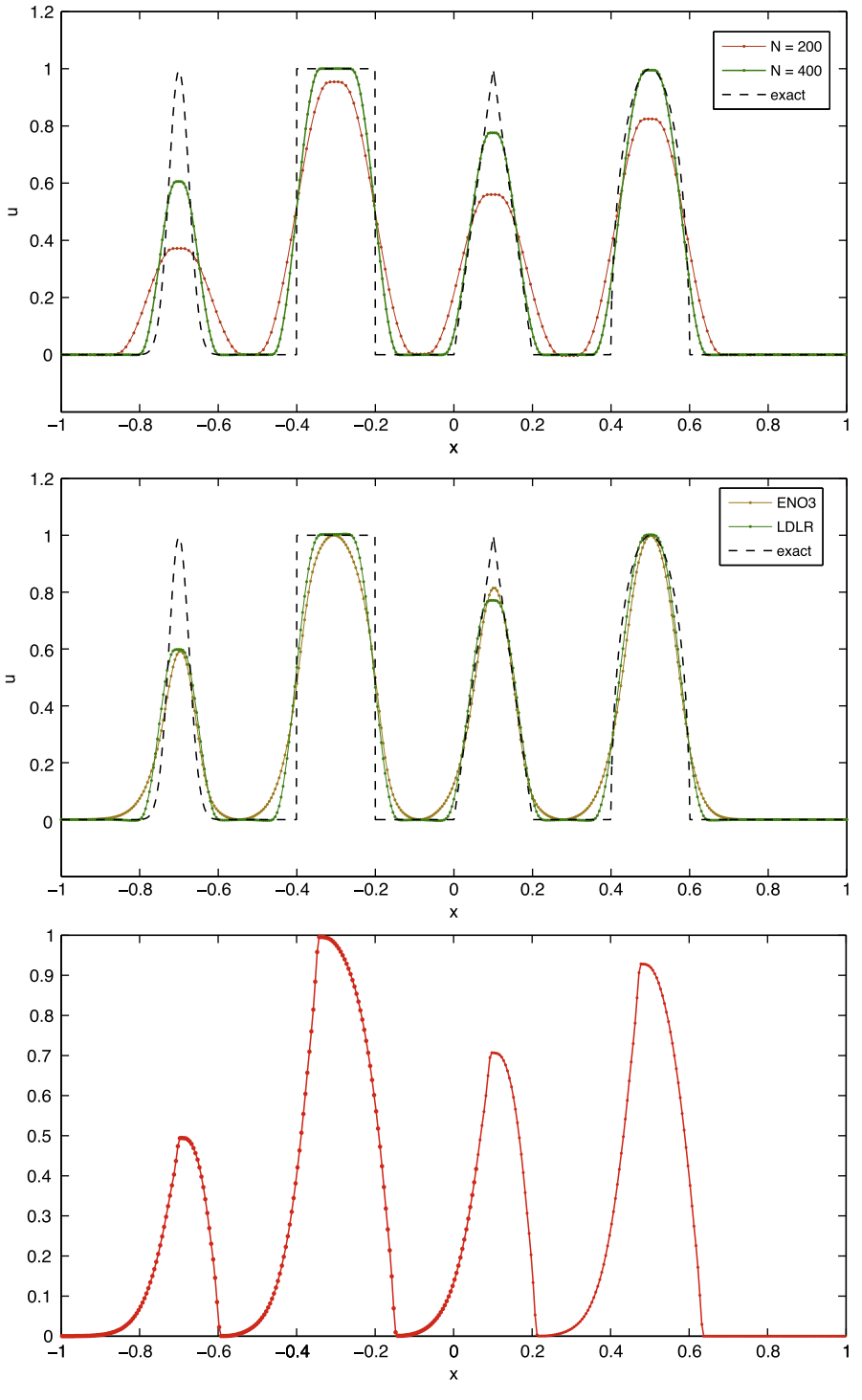


*5.1.3. Non-linear scalar equations*

It is our aim to examine the total variation for non-linear scalar equations. First we solve Burger's equation

$$u_t = -\left(\frac{u^2}{2}\right)_x, \quad u_0(x) = 1 + \frac{1}{2}\sin(\pi(x-1)) \tag{5.6}$$

on a periodic domain $x \in [-1,1]$ under CFL condition $\nu = 0.9$.

Second we calculate the non-convex Buckley–Leverett equation

$$u_t = -\left(\frac{u^2}{u^2 + a(1-u)^2}\right)_x, \quad u_0(x) = \begin{cases} 1 & \text{if } -\frac{1}{2} \leqslant x \leqslant 0, \\ 0 & \text{elsewhere} \end{cases} \tag{5.7}$$

on the same spatial domain and with the Courant number $\nu = 0.7$. The constant $a$ is set to $\frac{1}{4}$ and the initial profiles are taken from [5]. For the Buckley–Leverett equation we use the local Lax–Friedrichs flux

$$\mathcal{F}_{i+\frac{1}{2}}(\hat{u}^{(-)}, \hat{u}^{(+)}) = \frac{1}{2}\left(f(\hat{u}^{(-)}) + f(\hat{u}^{(+)}) - a_{i+1/2}(\hat{u}^{(+)} - \hat{u}^{(-)})\right), \tag{5.8}$$

with the wave propagation speed $a_{i+1/2} = \max\left(\left|\frac{\partial f(u)}{\partial u}\right|\right)$.

We calculate for both equations the total variation for a grid function $\bar{u}$

$$TV(\bar{u}^n) \equiv \sum_{i=1}^{N} |\bar{u}^n_{i+1} - \bar{u}^n_i| \tag{5.9}$$

of the discrete solution.

Fig. 11(left) shows the numerical behavior of the total variation for Burger's equation and the LimO3 approximation at $t = 2.0$. We observe that the calculated total variation is bounded by $TV(\bar{u}^0)$ and gradually decreases with time as a jump discontinuity forms at $t \approx 1.0$. In contrast to LDLR, the accuracy of the solution with 40 cells is significantly better (see [5]) and the evolving smooth profile for $t \in [0, 0.8]$ is recovered accurately. Note that for all three resolutions the value of total variation before the shock forms is always larger than that of LDLR. Hence the smooth profile is resolved more accurately with few computational cells. This could even be improved with a larger asymptotic region, yet also leading to larger, but bounded spurious oscillations shortly before the jump discontinuity forms. However once the discontinuity clearly appears the limiter yields $\phi^{\mathcal{O}(3)} \to \hat{\phi}(0) = 0$ and the oscillations completely disappear.

In the case of the Buckley–Leverett equation we analyze a very similar total-variation behavior (see Fig. 12). Although we introduce some spurious variation, which eventually diminishes as the mesh is refined. The slight overshoots at $x = 0.62$ in the compound wave are similar to the LDLR results (see [5] for details) and are not connected to the asymptotic region. Due to the compressible character of high-order schemes, the shock speed is approximated slower than the characteristic speed at some cells between the rarefaction and the shock. Adding diffusion, i.e., simply decreasing the parameter $\beta$ in $\hat{\phi}$ Eq. (3.9) damps out the spurious overshoot in the vicinity of the shock.

### 5.2. One-dimensional systems

The order of the scheme is based upon the reconstruction of the interface values and not upon the numerical flux function. Hence the proposed scheme is not tied to any particular flux function. Since our reconstruction is very efficient, we can choose a more costly – in terms of floating point operations – flux function. We formulate the numerical flux in terms of all the eigenvalues $\lambda_p$, eigenvectors $r_p$ and characteristic variables $\alpha_p$ of the Roe-averaged matrix [15]:

$$\mathcal{F}_{i+\frac{1}{2}}(\hat{u}^{(-)}, \hat{u}^{(+)}) = f(\hat{u}^{(-)}) + \sum_p \alpha_p |\lambda_p| r_p. \tag{5.10}$$

All calculation are performed with the limiter function applied on conservative variables in order to keep the new method as simple and efficient as the TVD-MUSCL scheme.

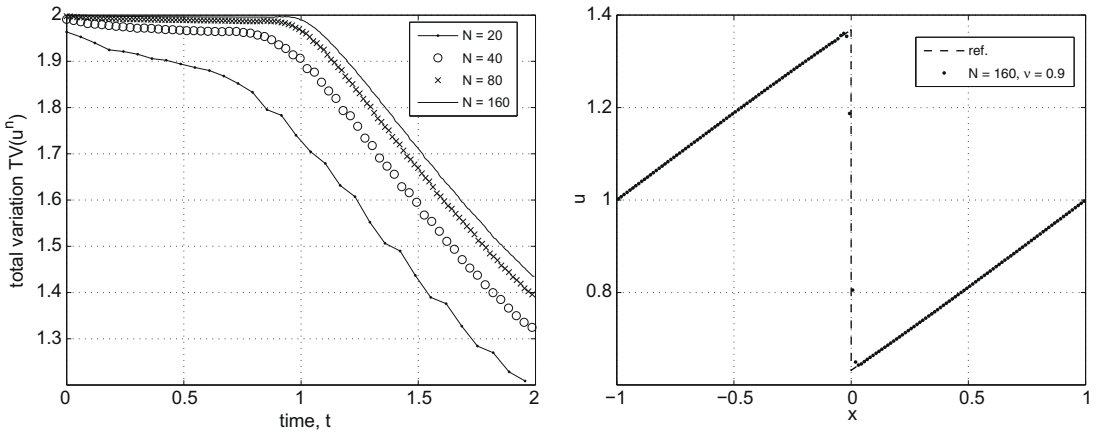


**Fig. 11.** Total variation of Burger's equation (left) and LimO3 approximation with $\nu = 0.9$ and $r = 0.1$ at $t = 2.0$.

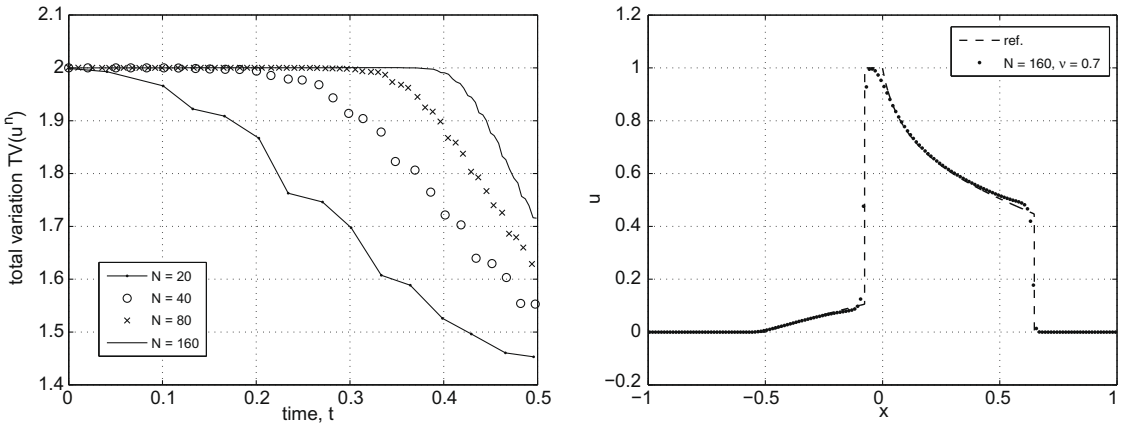


**Fig. 12.** Total variation of the Buckley–Leverett equation (left) and LimO3 approximation with $v = 0.7$ and $r = 0.1$ at $t = 0.4$.

*5.2.1. Gas dynamics: 1D Euler equations*

We consider an inviscid, compressible and non-heat conducting gas modeled by the Euler equations:

$$\partial_t \begin{pmatrix} \rho \\ \rho v \\ E \end{pmatrix} + \partial_x \begin{pmatrix} \rho v \\ \rho v^2 + p \\ v(E+p) \end{pmatrix} = 0, \tag{5.11}$$

where $\rho$ is the density, $p$ is the pressure and $v$ is the velocity, respectively. We assume a polytropic gas with the total energy

$$E = \frac{1}{2}\rho v^2 + \frac{1}{\gamma - 1} p, \tag{5.12}$$

where $\gamma$, the adiabatic exponent, i.e., the ratio of specific heat, is set to be 1.4 for diatomic gases. We compute initial value problems by means of an initial profile of the primitive variables $\rho$, $v$, and $p$ defined through the domain.

*5.2.2. Non-linear traveling plane waves*

In order to calculate the empirical order of convergence (EOC) for non-linear systems, we have chosen a non-linearly coupled test problem, which develops a shock profile. We consider a convergence test on periodic boundaries $x \in [0, 1]$ with initial conditions

$$\begin{pmatrix} \rho \\ v \\ p \end{pmatrix}_0 = \begin{pmatrix} \left(1 + \frac{1}{2}(\gamma - 1)\frac{v_0}{c_0}\right)^{\kappa} \\ 1/4 \sin(\pi x) \\ \left(1 + \frac{1}{2}(\gamma - 1)\frac{v_0}{c_0}\right)^{\gamma\kappa} \end{pmatrix}, \quad c_0 = \sqrt{\gamma}, \quad \kappa = \frac{2}{\gamma - 1}. \tag{5.13}$$

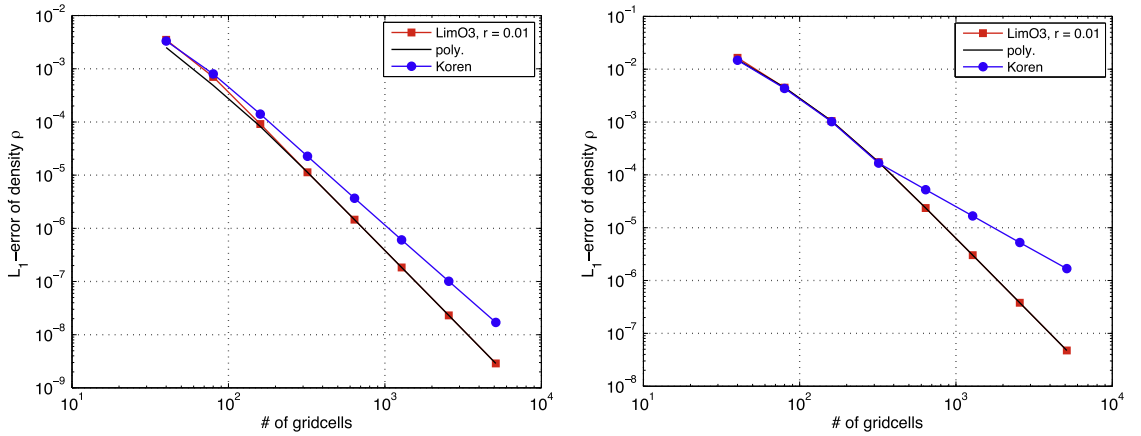


**Fig. 13.** EOC density profile of a non-linear plane wave for the Euler equations at $t = 0.8$ with $v = 0.8$ and $r = 0.01$. Koren limiter $\phi^{\mathrm{TVD}}(\theta)$ Eq. (3.11) with $v = 0.8$.

The initially smooth flow will eventually steepen and form a shock wave at $t^{\star} = \frac{8}{\pi(\gamma+1)} \approx 1.06$ [14]. This way the EOC reflects the accuracy of the whole scheme, including a linearized approximated Riemann solver.

In Fig. 13 we have plotted the calculated errors in the density component at $t = 0.8$. We compare the proposed algorithm RK3rd, LimO3 $\phi^{\mathcal{O}(3)}(\delta_{i-1/2}, \delta_{i+1/2})$ Eq. (3.22) with RK3rd, Koren limiter $\phi^{\mathrm{TVD}}(\theta)$ Eq. (3.11). A reference solution is obtained with the third-order unlimited polynomial reconstruction Eq. (3.1) using 40,960 cells. Due to the rather flat initial density profile we get almost optimal accuracy with already 40 computational cells having $r = 0.01$. Similar to the previous convergence experiment (see Fig. 9) both schemes exhibit nearly identical accuracy on coarse grids. Once the resolution is sufficient refined the asymptotic region is switched on and $\phi^{\mathcal{O}(3)}(\delta_{i-1/2}, \delta_{i+1/2})$ Eq. (3.22) recovers full third-order accuracy. Yet the Koren limiter always smears out smooth structures.

*5.2.3. Riemann problem: shock–blast interaction*

In this rather challenging problem, suggested as benchmark in [35], two blast waves collide and generate multiple strong shocks and rarefactions in the computational domain $x \in [0, 1]$. Classical second-order TVD limiters, such as super-bee are either too compressive and produce negative density or they are too diffusive and smear out the contact waves and local extrema. The initial data for the simulation consist of three constant states:

$$(\rho, v, p)_0 = \begin{cases} (1, 0, 10^3), & 0 \leqslant x < 0.1, \\ (1, 0, 10^{-2}), & 0.1 \leqslant x < 0.9, \\ (1, 0, 10^2), & 0.9 \leqslant x \leqslant 0.1. \end{cases} \tag{5.14}$$

Reflecting boundary conditions are applied at both ends of the domain and the solution is evolved until $t = 0.038$ with $r = 1.0$. Figs. 14 and 15 compare the density, total energy and pressure profiles computed on a 800 cell grid with reference and LDLR data from Artebrant and Schroll [5].

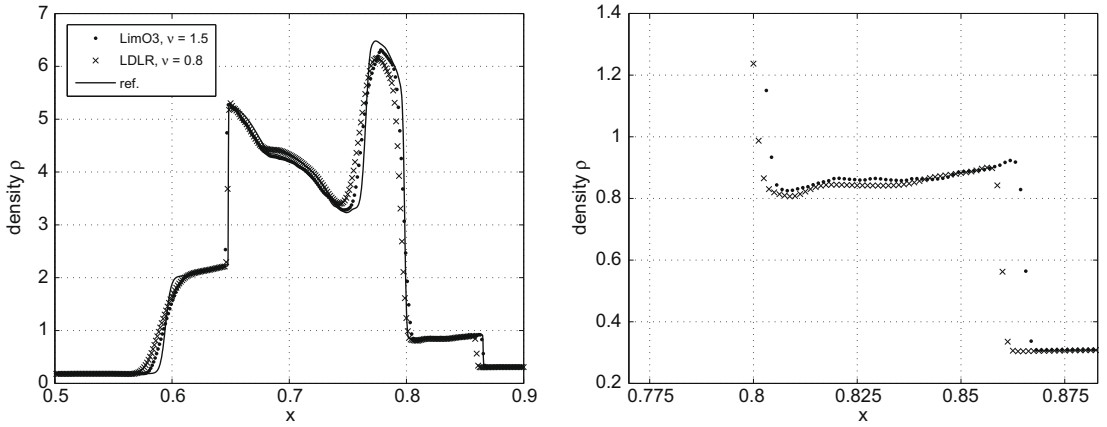

The results obtained with the new scheme LimO3 with Courant number $\nu = 1.5$ approximates the solution more accurately than LDLR. In both the density and the energy distribution we can clearly observe a better resolution of the local extrema in the middle of the domain. The shock is resolved sharply within only two cells without any spurious oscillations and with the correct velocity. The left contact discontinuity is also very accurately approximated.

The Koren limiter failed on this experiment. The calculation eventually broke down, producing unphysical densities when the two reflected shocks collided together in the middle of the domain. We suspect that the Koren limiter is too compressive for this experiment. Similar observations have been made with the second-order accurate, but compressive super-bee limiter.

*5.2.4. Riemann problem: shock–acoustic-wave interaction*

This test case was proposed in [24]. It simulates an interaction of a supersonic shock wave with a sinusoidal density disturbance involving smooth structures and a sharp shock. A Mach 3 shock wave moves into a smooth acoustic wave, which gets amplified and has higher frequency right behind the shock. We solve the 1D Euler equation on the domain $x \in [-5, 5]$ with constant extrapolating boundary conditions. The initial conditions are prescribed as

$$(\rho, v, p)_0 = \begin{cases} (3.857143, 2.629369, 10.333333), & x < -4, \\ (1 + 0.2\sin(5x), 0, 1), & x \geqslant -4. \end{cases} \tag{5.15}$$

In Fig. 16 we show computational results for the density component obtained at $t = 1.8$ using 400 FV-cells. We compare the solution for the proposed algorithm LimO3 with LDLR results from Artebrant and Schroll [5] (Fig. 16, right) and with the Koren limiter (Fig. 16, left). Since the solution is dominated by smooth, but narrow structures we could expand the asymptotic region Eq. (3.17) setting the radius $r = 1, r = 5$ and $r = 10$. The effect is clearly visible. The local extrema in $x \in [0.5, 2]$ are considerably better resolved increasing $r$ and are perfectly symmetric. We have to note that we could also run this Riemann problem without any limiting procedure, hence using the full parabolic spatial reconstruction, Fig. 17(left). Similar to the

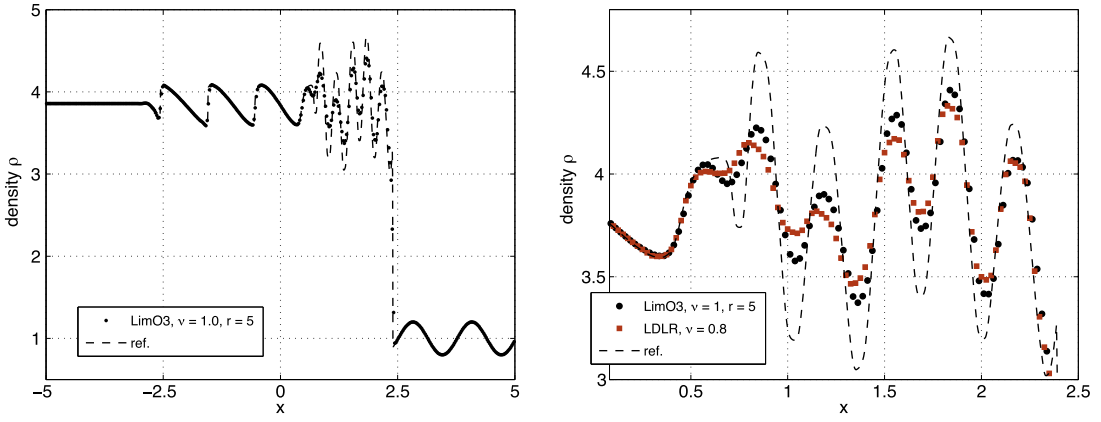


**Fig. 16.** Density distribution of Shu–Osher shock-acoustic test case for Euler equations. Comparison at $t = 1.8$ of LimO3 ($r = 5$) and LDLR using 400 cells.

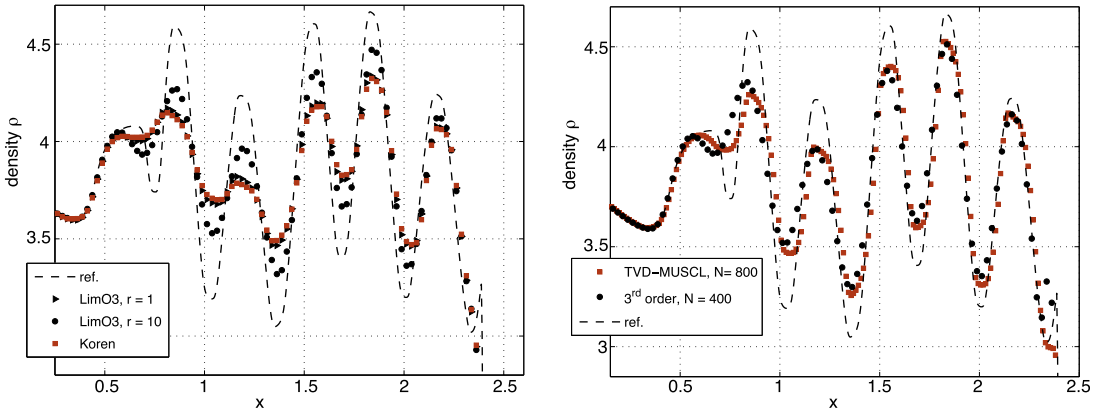


**Fig. 17.** Density distribution of Shu–Osher shock-acoustic test case for Euler equations at $t = 1.8$. Left: Comparison of Koren limiter and LimO3 with $r = 1$ and $r = 10$ using 400 grid cells. Right: Comparison of unlimited quadratic reconstruction Eq. (3.1) using 400 cells and second-order TVD-MUSCL scheme with van Leer's limiter Eq. (5.16) with 800 cells.

observation we have made for the linear advection equation (see Fig. 8) the unlimited third-order reconstruction remains stable with minor over- and under-shoots in the vicinity of the shock, hence allowing us to choose a large asymptotic region. This is in contrast to classical second-order method, which could not simulate this experiment without proper TVD limiters. Yet even compressive TVD limiters, such as van Leer's harmonic mean limiter [15]

$$\phi^{vL}(\theta) = \frac{\theta + |\theta|}{1 + \theta} \tag{5.16}$$

needs around twice as many computational cells to resolve the smooth structure behind the shock, Fig. 17(right).

Note that if we set $r \leqslant 1$ we obtain qualitatively similar results to LDLR and the Koren limiter. However in contrast to LDLR we produce no under-shoots in the region with steep gradients $x \in [-2, 0]$. This is identical to the Koren limiter, which always limits steep gradients to first-order. It is an advantage of our reconstruction, that we do not change the TVD property of the limiter $\phi^{O(3)}(\delta_{i-1/2}, \delta_{i+1/2})$ Eq. (3.22) once a discontinuity is detected, i.e., the function $\hat{\phi}(\theta)$ is switched on. Enlarging the asymptotic region allows, already on a coarse mesh, the consideration of data with large curvature as smooth structures. This is different in the LDLR scheme. There the total variation-control parameter $q$ has to be decreased. This eventually leads to an improved resolution of the smooth profile in $x \in [0.4, 2.4]$, but also to a more variation in the vicinity of discontinuities, because variation is introduced everywhere.

### 5.3. Magnetohydrodynamics (MHD)

We extend our 1D system to the ideal MHD equations, which model the dynamics of plasma. Plasma dynamics are influenced by magnetic fields induced through the Lorentz-force. Therefore an additional evolution equation for the magnetic field $\boldsymbol{B}$ has to be derived. Further terms in the Euler system Eq. (5.11) which quantify magnetic force and energy density are also needed. The adiabatic constant is $\gamma = 5/3$. The whole MHD system including the approximated Riemann solver can be found in, e.g. [28,29] (and references therein).

The intention of this section is twofold. First we consider a convergence test to prove the formal order of our scheme for a non-linear rather complicated system. Second we compare the non-uniform converge for one-dimensional MHD Riemann problems for different schemes.

#### 5.3.1. Empirical order of convergence (EOC)

We solve the MHD equations on the domain $x \in [-1, 1]$ with smooth initial data [4], $\rho = 1.5 + 0.5\sin(\pi x)$, $v_x = 1.5 + 0.25\cos(\pi x)$, $v_y = 1.5 + 0.25\sin(\pi x)$, $B_x = 0.5$, $B_y = 1.0$ and $p = 0.25$. The errors are calculated for $t = 0.628$ using a reference solution obtained on a very fine grid with the pure quadratic reconstruction Eq. (3.1). We compare the convergence rate of both LimO3 and LDLR methods to envisage the particular difference of the radius $r$ in the proposed asymptotic domain and the variation-control parameter $q$ of LDLR.

Fig. 18 shows the calculated empirical convergence error for the density distribution of the LimO3 scheme for various radii of the asymptotic region. In Fig. 19 we envisage the empirical convergence error of LDLR. LDLR has been implemented as described in [5]. Both methods need around 200 FV-cells to reach the desired convergence error since the smooth extrema in the density profile are rather narrow. However LimO3 converges always faster, i.e., using less grid cells, than LDLR. In addition for $r = 1.0$ and $r = 0.5$ the convergence error is clearly smaller than for LDLR with $q = 1.0$. Remember for $q \to 0$, LDLR recovers the pure quadratic polynomial. Though the most important difference is that even for a small radius of the asymptotic region we clearly see the correct convergence error. Whereas LDLR with the variation-control-exponent $q = 1.0$ needs more than 5000 FV-cells to converge to the error of pure quadratic reconstruction. In other words with changing the radius

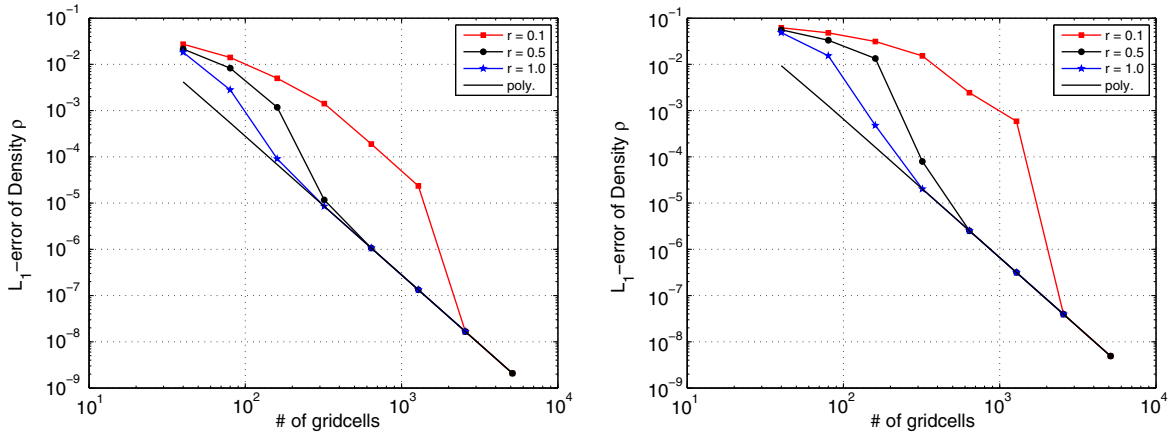


**Fig. 18.** EOC of LimO3 for the 1D MHD system at $t = 0.628$ with $v = 0.8$ and different asymptotic regions.

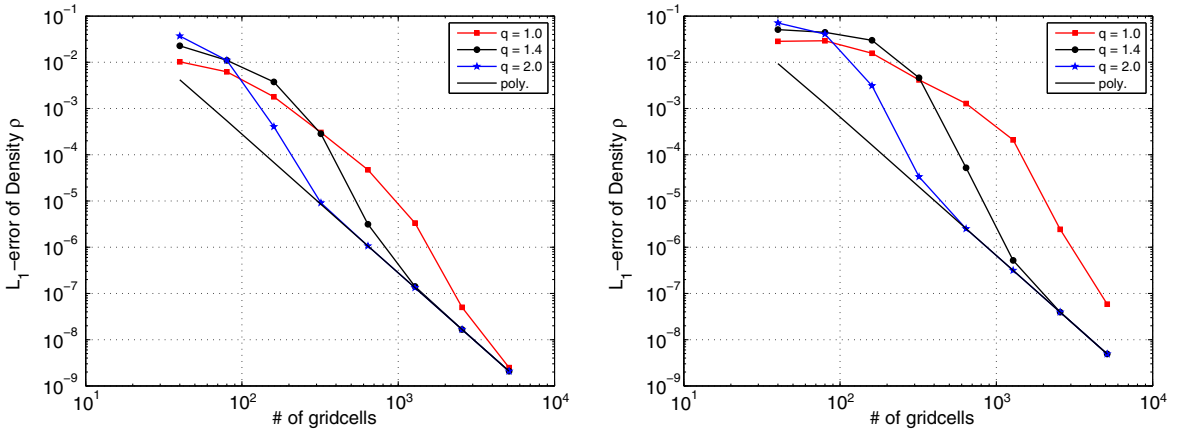


**Fig. 19.** EOC of LDLR for the 1D MHD system at $t = 0.628$ with $v = 0.8$ and different variation-control parameters $q$.

of the asymptotic region we just change the ability of the new limiter $\phi^{\mathcal{O}(3)}(\delta_{i-1/2}, \delta_{i+1/2})$, to distinguish between local smooth extrema and discrete gradients with one vanishing lateral derivative. But once a discontinuity is recognized the limiter $\hat{\phi}(\theta)$ diminishes total variation. Changing the variation-control parameter $q$ in LDLR affects the whole reconstruction procedure. A small $q$ increases the total variation (decreases the diffusion), yet the reconstruction cannot accurately recover smooth extrema with one vanishing lateral derivative. For $q > 1.4$ the total variation is significantly decreased, yet diffusion is also increased, but the LDLR algorithm can resolve smooth extrema with one vanishing lateral derivative more accurately. This is a significant difference of both schemes. Our aim is primarily to retain the very good shock capturing properties of the $\hat{\phi}(\theta)$ limiter and yet to be able to accurately resolve smooth structures with one vanishing lateral derivative.

*5.3.2. Pseudo convergence*

We consider an almost coplanar Riemann problem, as proposed in [28], to investigate the convergence properties towards the true solution. It has been described in detail for several second-order methods in [28] and for very high, up to a ninth-order method, in [29] that all schemes converge initially to a wrong solution. Only with a very fine spatial resolution the methods start to converge to the right solution. As such, the Riemann problem is a hard test case for FV methods. The aim is to recover the correct convergence on a coarse computational grid.

We investigate the error of the numerical solution obtained by the proposed method LimO3 and compare it to three different methods: A second-order method (Roe2) with $v = 0.9$ (see [28]), a fifth-order WENO (WENO5) scheme with $v = 0.4$ (see [29] and references therein), and the LDLR method with $v = 0.9$. Roe2, LimO3 and LDLR are conducted with the same approximated Riemann solver and the higher-order methods, LimO3, LDLR and WENO5 use the same explicit three-stage Runge–Kutta time-marching scheme. The second-order TVD Heun time-marching scheme is implemented in Roe2.

The left picture in Fig. 20 shows the convergence results of the magnetic field $B_y$ for an almost coplanar Riemann problem consisting only of regular waves (r-solution), i.e., shock and discontinuities. The solution for the Riemann problem consisting

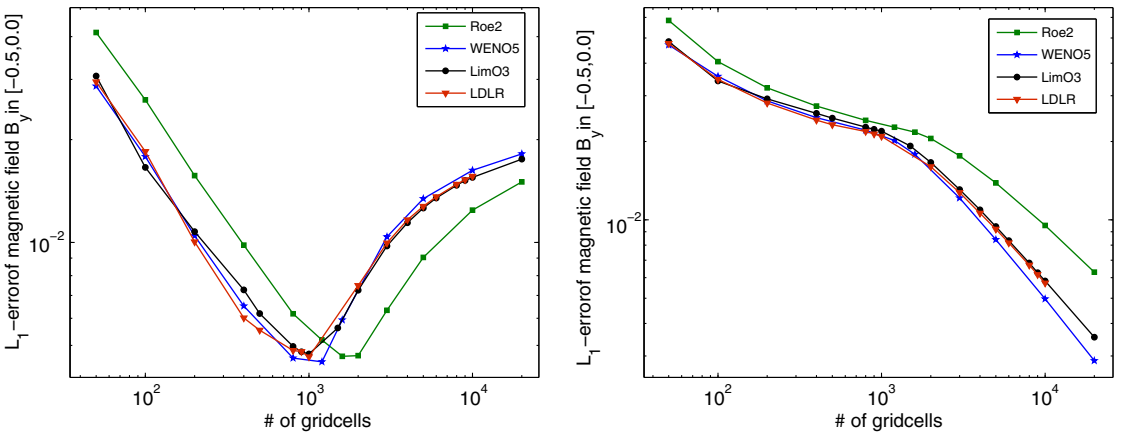


**Fig. 20.** Almost coplanar MHD Riemann problem. $L_1$-errors of the magnetic field $B_y$ for the twist angle $\alpha = 3.0$ with respect to the c-solution (left) and r-solution (right). Lim03 has $v = 1.5$ and $r = 0.5$.

of any non-regular waves, c-solutions for compound waves, is shown in the right picture of Fig. 20. LimO3, LDLR and WENO5 exhibit eventually the same results. All three methods start to converge with the same accuracy from 1000 cells upwards to the true solution. As already concluded in [29] very high order, such as WENO5, does not significantly improve the pseudo convergence although they display smaller numerical viscosity than second-order TVD methods (Roe2). Note that LimO3 qualitatively computes the same numerical solution as WENO5, yet using a nearly four times higher Courant number $v = 1.5$ and only three data points for spatial reconstruction. Changing the radius of the asymptotic region did not improve the pseudo convergence.

### 5.4. Euler system in two dimensions

We compute 2D experiments using a dimension by dimension reconstruction approach

$$\frac{d}{dt}\bar{u}_{ij} = L_i(\bar{u}_j) + L_j(\bar{u}_i) = \frac{1}{\Delta x}\left(\mathcal{F}_{i-\frac{1}{2}j} - \mathcal{F}_{i+\frac{1}{2}j}\right) + \frac{1}{\Delta y}\left(\mathcal{G}_{ij-\frac{1}{2}} - \mathcal{G}_{ij+\frac{1}{2}}\right). \tag{5.17}$$

We recover the intermediate values $\hat{u}^{(\pm)}_{i\pm\frac{1}{2}j}$ and $\hat{u}^{(\pm)}_{ij\pm\frac{1}{2}}$ with the proposed third-order reconstruction applied on the conserved variables using the HLLE approximated Riemann solver [27]. Since the flux evaluation is done in both directions in every single Euler stage of the third-order Runge–Kutta method, the stability criterion yields:

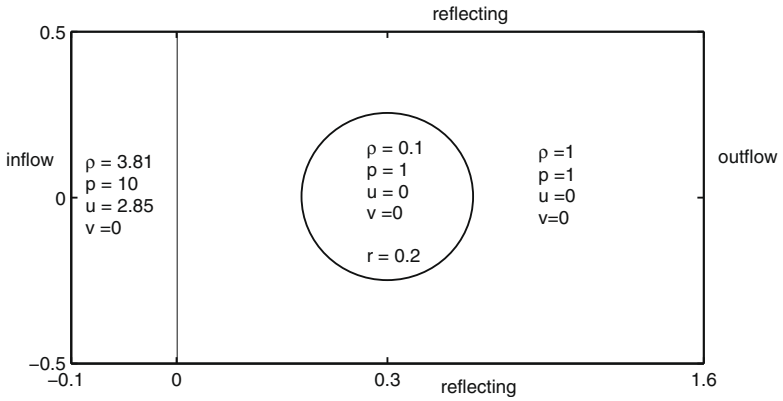


**Fig. 21.** Shock-bubble experimental setup for 2D Euler equation.

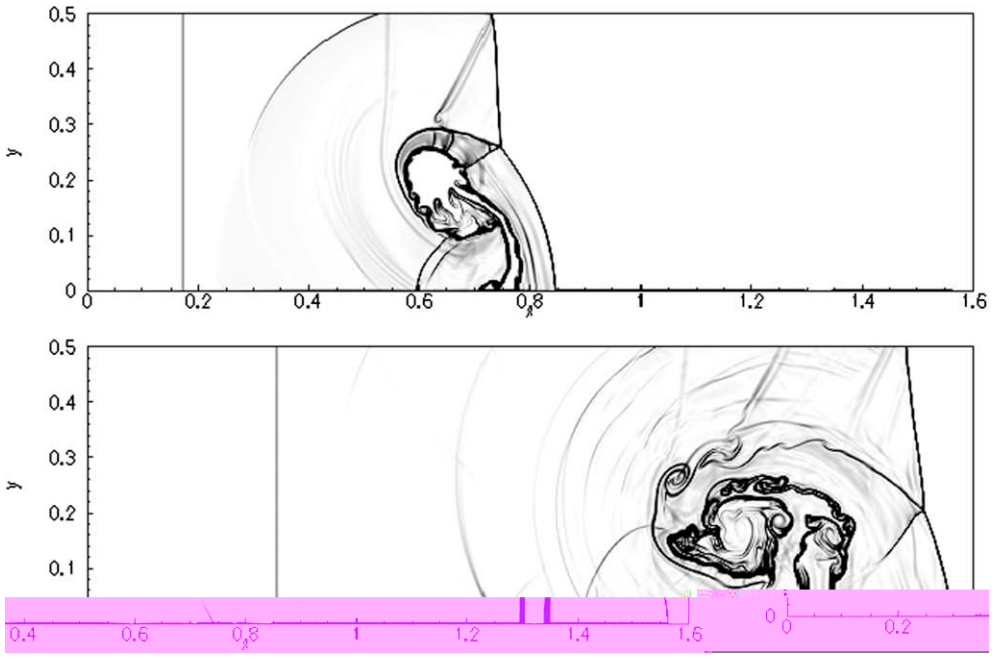


**Fig. 22.** Emulated Schlieren picture of shock-bubble simulation with 1700 × 500 cells with $v = 1.5$. Top: $t = 0.2$. Bottom: $t = 0.4$.

$$v = 0.5(v_x + v_y) \leqslant 1.6. \tag{5.18}$$

We compare the following three schemes:

| | |
|---|---|
| TVD-MUSCL | Heun $\mathcal{O}(\Delta t^2)$ with van Leer's harmonic limiter $\phi^{vL}(\theta)$ Eq. (5.16) |
| RK3rd, LimO3, $r = 1.0$ | RK3rd $\mathcal{O}(\Delta t^3)$ with limiter $\phi^{\mathcal{O}(3)}(\delta_{i-1/2}, \delta_{i+1/2})$ Eq. (3.22) |
| RK3rd, Koren | RK3rd $\mathcal{O}(\Delta t^3)$ with Koren limiter $\phi^{\text{TVD}}(\theta)$ Eq. (3.11) |

*5.4.1. Shock-bubble*

In this experiment we simulate a strong rightwards moving shock wave over a low density gas bubble. The initial condition and the experiment geometry are sketched in Fig. 21. As the problem is symmetric we compute the upper part $y \geqslant 0$ only and specify reflecting boundary conditions at $y = 0$ and inflow boundary condition at $x = -0.1$.

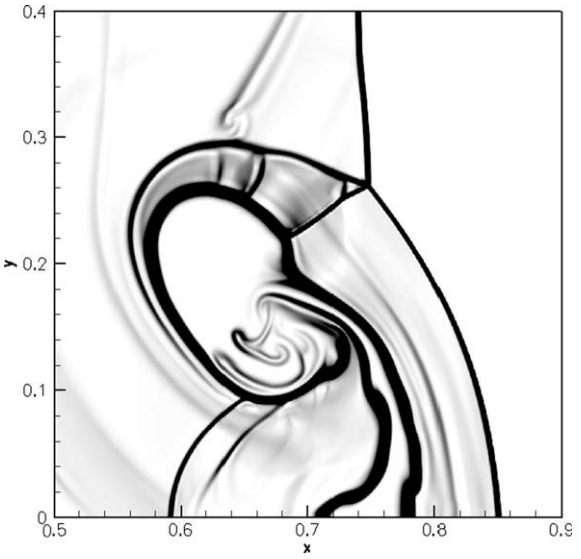


**Fig. 23.** Zoom of the shock-bubble Schlieren image Fig. 22. Second-order TVD-MUSCL scheme with van Leer's limiter Eq. (5.16) with $v = 0.9$ at $t = 0.2$.

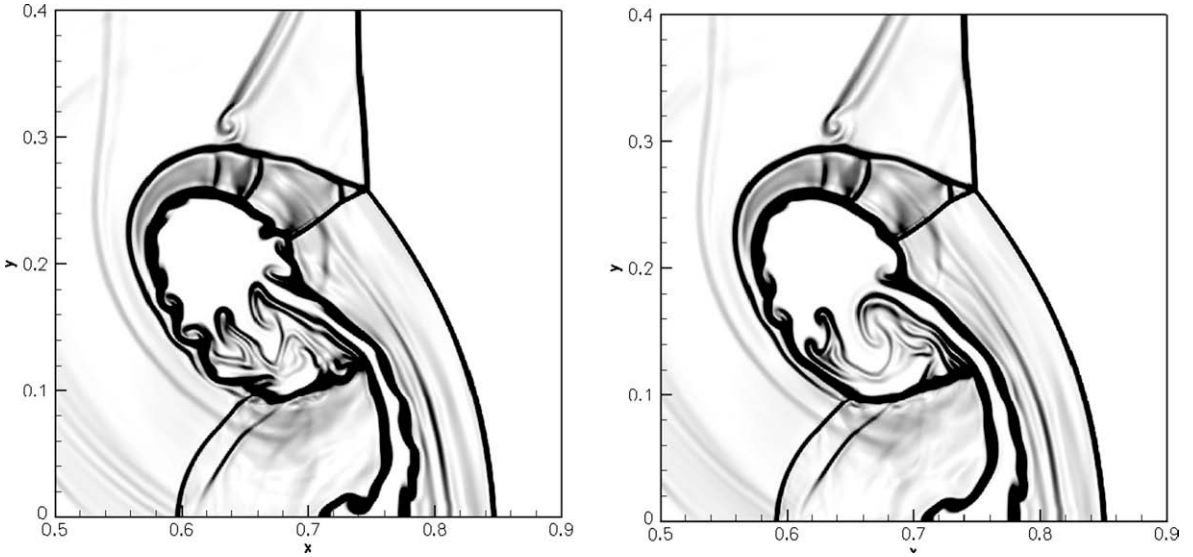


**Fig. 24.** Zoom of the shock-bubble Schlieren image Fig. 22. Left: LimO3 ($r = 1.0$) with $v = 1.5$. Right: Koren limiter $\phi^{\text{TVD}}(\theta)$ Eq. (3.11) with $v = 1.5$.

The LimO3 and van Leer's TVD-MUSCL approximations are computed on a uniform mesh consisting of $1700 \times 500$ FV-cells. LimO3 results are obtained using $v = 1.5$ with $r = 1.0$, whereas the TVD-MUSCL scheme has $v = 0.9$.

Fig. 22 shows the numerical results of LimO3 at different times. The emulated Schlieren pictures display density gradients on a grey scale. In Figs. 23 and 24 the results at $t = 0.4$ are compared for all three methods, namely TVD-MUSCL, LimO3 and Koren limiter. We observe more small scale vortexes in the approximation of LimO3. The contact discontinuities are resolved more accurately with the third-order method LimO3, still remaining computationally as fast as the second-order TVD-MUSCL scheme. Although the accuracy of the solution is already improved with the Koren limiter (Fig. 24, right), considerably more details are still captured with LimO3 (Fig. 24, left).

*5.4.2. 2D Riemann problem: Euler-four-shocks*

We have taken two 2D Riemann problems originally defined in [20]. Both problems are solved on a square domain $(x, y) \in [0, 1] \times [0, 1]$, with initial constant states in four quadrants. The first Riemann problem features four shock waves with the contact point localized at (3/4, 3/4) as proposed by [21]:

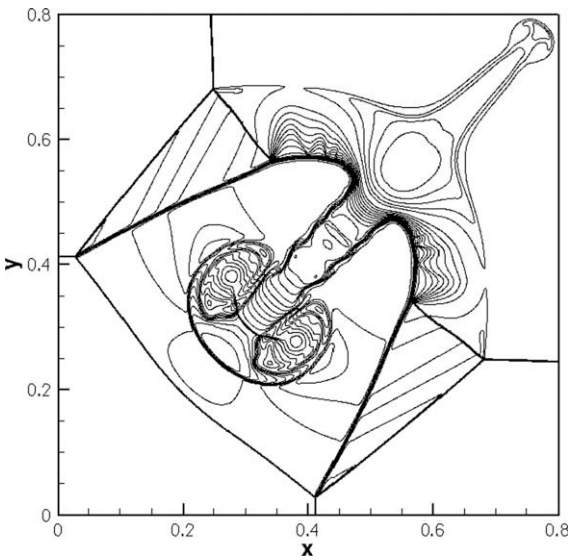


**Fig. 25.** Density contour plot of Euler-four-shocks problem using $1000 \times 1000$ cells at time 0.8. Second-order TVD-MUSCL scheme with van Leer's limiter Eq. (5.16) and $v = 0.8$.

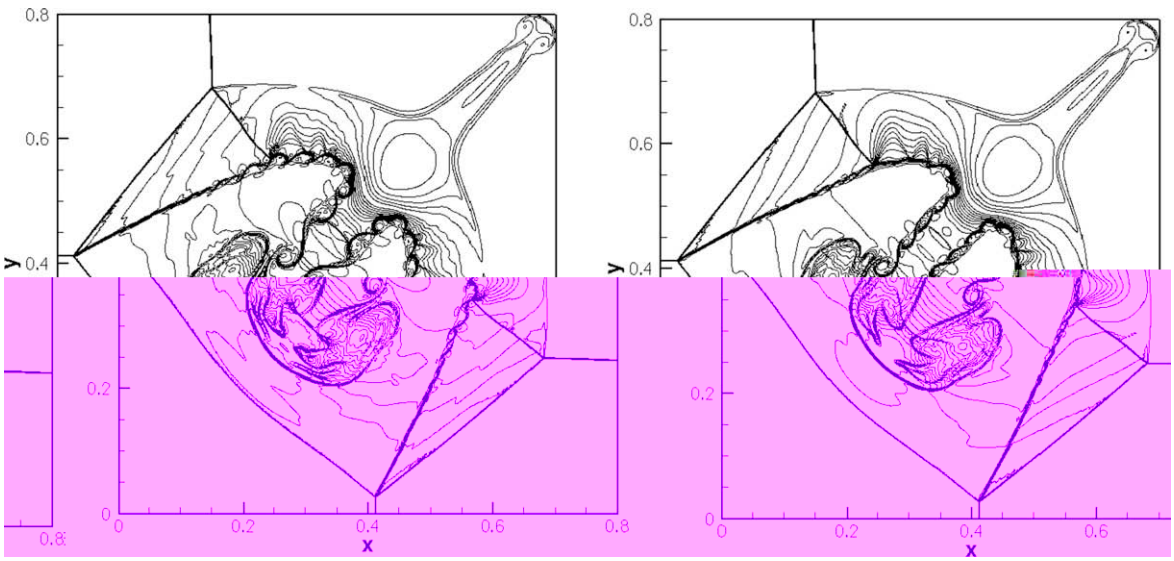


**Fig. 26.** Density contour plot of Euler-four-shocks problem using $1000 \times 1000$ cells at time 0.8. Left: LimO3 with $v = 1.5$ and $r = 1.0$. Right: Koren limiter $\phi^{\mathrm{TVD}}(\theta)$ Eq. (3.11) with $v = 1.5$.

$$(\rho, u, v, p)_0 = \begin{cases} (1.5, 0, 0, 1.5), & [0.75, 1] \times [0.75, 1], \\ (0.5323, 1.206, 0, 0.3), & [0, 0.75) \times [0.75, 1], \\ (0.138, 1.206, 1.206, 0.029), & [0, 0.75) \times [0, 0.75), \\ (0.5323, 0, 1.206, 0.029), & [0.75, 1] \times [0, 0.75). \end{cases} \tag{5.19}$$

We compare in Figs. 25 and 26 density contour profiles of all three schemes. The numerical solution is obtained at $t = 0.8$ with a Courant number of $v = 1.5$ for LimO3 and Koren limiter and $v = 0.8$ for van Leer's TVD-MUSCL scheme on a uniform grid with $1000 \times 1000$ cells. All boundaries are artificial boundaries, i.e., constant extrapolated. Similar to the previous experiment the amount and quality of details of the solution increases with the accuracy of the scheme. All three approximations obtain the basic structure of the solution where the four shock waves interact. However LimO3 still resolves the contact discontinuity and the middle and top right plume with more details. The LimO3 and Koren limiter results are perfectly symmetric. For less accurate resolution the differences between all three methods where less profound. LimO3 needs sufficient high resolution for small-scale structures, since the asymptotic region $\eta(\delta_{i-1/2}, \delta_{i+1/2})$ Eq. (3.17) is mesh size dependent. On coarse grids the solutions obtained with LimO3 and Koren limiter are of similar quality. Note that the LimO3 sim-

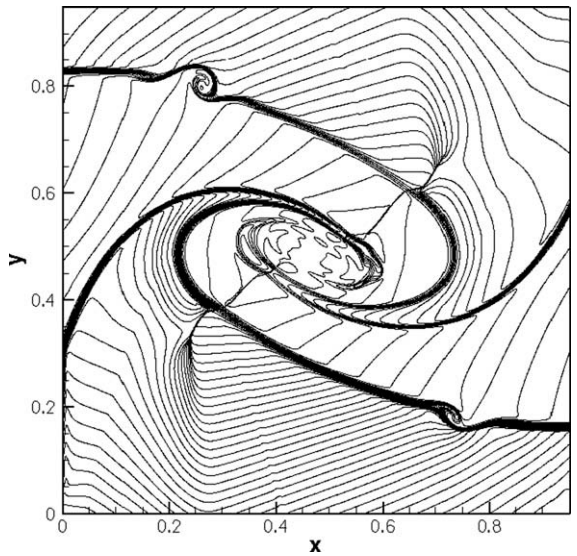


**Fig. 27.** Density contour plot of Euler-four-contacts problem using $1000 \times 1000$ cells at time 0.8. Second-order TVD-MUSCL scheme with van Leer's limiter Eq. (5.16) and $v = 0.8$.

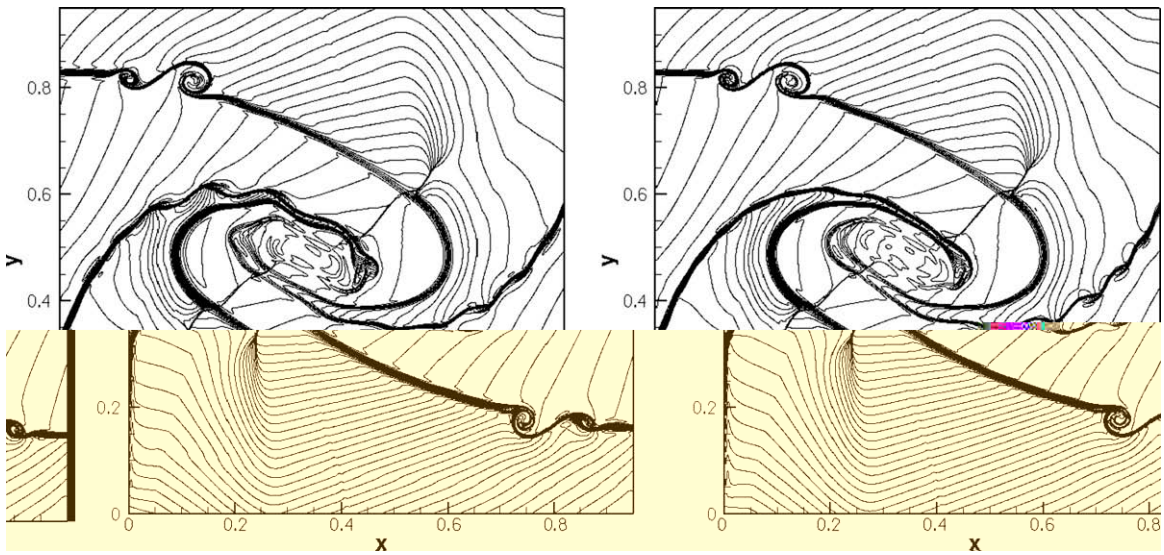


**Fig. 28.** Density contour plot of Euler-four-contacts problem using $1000 \times 1000$ cells at time 0.8. Left: LimO3 with $v = 1.5$ and $r = 1.0$. Right: Koren limiter $\phi^{\text{TVD}}(\theta)$ Eq. (3.11) with $v = 1.5$.

ulation is, because of Courant number $\nu = 1.5$, as fast as the second-order accurate TVD simulation, yet essentially of third-order accuracy in smooth regions. For comparison with different hight-order schemes see [16].

*5.4.3. 2D Riemann problem: Euler-four-contacts*

This Riemann problem consists of two shock waves generated at the origin of the domain (see Figs. 27 and 28). The structure of the solution has the quality of a vortex turning clockwise. The initial conditions are:

$$(\rho, u, v, p)_0 = \begin{cases} (1, 0.75, -0.5, 1), & [0.5, 1] \times [0.5, 1], \\ (2, 0.75, 0.5, 1), & [0, 0.5) \times [0.5, 1], \\ (1, -0.75, 0.5, 1), & [0, 0.5) \times [0, 0.5), \\ (3, -0.75, -0.5, 1), & [0.5, 1] \times [0, 0.5). \end{cases} \tag{5.20}$$

The generated shock waves propagate outwards following the slip lines, which are spiraled around the origin. We evolve the initial data until $t = 0.8$ on a uniform grid with $1000 \times 1000$ cells. Similar to the previous experiments LimO3 (Fig. 28 – left) exhibits the most detailed self-similar solution. Comparing Figs. 27 and 28, we can clearly observe a better resolved vortex at the top and bottom. LimO3 resolves the contacts with more details. The second-order accurate MUSCL scheme is not symmetric. For comparison with different high-order methods see [22].

## 6. Conclusions

In this paper we have derived and analyzed a new third-order limiter for the numerical solution of hyperbolic conservation laws. In contrast to classical second-order TVD limiters, the proposed limiter function maintains its formal accuracy at local extrema. Yet remaining still a simple, efficient piecewise-linear $(\max, \min)$ function. It acts as a logical switch depending on the left and right slope and avoids complicated and costly reconstruction techniques. The new limiter uses a local piecewise-parabolic reconstruction for smooth data and preserves accuracy within the asymptotic region. Similarities to limiter functions obeying Harten's TVD conditions have been analyzed. The new algorithm uses, in contrast to second-order methods, an explicit third-order Runge–Kutta time-marching scheme. Clear advantages in the frequency domain and less restrictive conditions for numerical stability for this time-marching method could be shown.

Various numerical experiments indicate the superiority of the proposed limiter over classical second-order TVD limiters. The new scheme also compares favorably with third-order methods such as LDLR, ENO3 and the Koren limiter. It has very good shape-preserving properties and known limiter effects, such as smearing and squaring do not appear. Numerical simulations with Courant numbers up to $\nu = 1.6$ make the proposed method just as efficient as classical second-order TVD-MUSCL schemes, yet significantly improving the result. Note that TVD methods are computationally more economical than ENO schemes [24]. Costly optimal stencil searches and memory storage are avoided.

## Acknowledgment

The authors thank Robert Artebrant for many fruitful discussions about reconstruction techniques in finite volume methods and for kindly providing us with his data.

## Appendix A. Derivation of the logarithmic limiter

In order to derive the logarithmic limiter Eq. (3.6) we have to formulate the cell interface values of LDLR as function of the smoothness measurement $\theta$ Eq. (2.8). The mesh size independent cell interface values of the LDLR are given by:

$$\hat{u}^{(\mp)}_{i\pm 1/2} = \bar{u}_i + c\eta^{(\pm)}(a) + d\eta^{(\pm)}(b), \tag{A.1}$$

where $a, b, c$ and $d$ are explicit function of the left and right slopes [5]:

$$a(\delta_{i-1/2}, \delta_{i+1/2}) = 1 - 2\frac{|\delta_{i-1/2}|^q |\delta_{i+1/2}|^q}{|\delta_{i-1/2}|^{2q} + |\delta_{i+1/2}|^{2q}} = 1 - 2\frac{|\theta|^q}{1 + |\theta|^{2q}}, \quad \delta_{i+1/2} \neq 0 \tag{A.2}$$

We define a function depending solely on the slope ratio $\theta$ (see Eq. (3.7))

$$p = p(\theta) \equiv 1 - a. \tag{A.3}$$

The functions $b, c$ and $d$ are algebraic expressions of $a(\delta_{i-1/2}, \delta_{i+1/2})$ and the left and right slopes. The logarithm functions come into the reconstruction via the functions [5]:

$$\begin{aligned} \eta^{(+)}(z) &= -\frac{\ln(1-z) + z}{z^2}, \\ \eta^{(-)}(z) &= \frac{(z-1)\ln(1-z) - z}{z^2}. \end{aligned} \tag{A.4}$$

We can reformulate all these functions in terms of $\theta$ and $p(\theta)$:

$$b = \frac{a}{a-1} = \frac{p-1}{p}, \tag{A.5}$$

$$c = \frac{(a-1)(\delta_{i+1/2}(1-b) - \delta_{i-1/2})}{b-a} = \frac{p-\theta p^2}{1-p^2}\delta_{i+1/2}, \tag{A.6}$$

$$d = \delta_{i-1/2} - c = \left(\theta - \frac{p-p^2\theta}{1-p^2}\right)\delta_{i+1/2}, \tag{A.7}$$

$$\eta(a)^{(+)} = -\frac{\ln(p)+1-p}{(1-p)^2}, \tag{A.8}$$

$$\eta(a)^{(-)} = \frac{(-p)\ln(p)-1+p}{(1-p)^2}. \tag{A.9}$$

To recover Eq. (3.5) with a single logarithmic limiter function Eq. (3.6), we have to plug in the above equations into Eq. (A.1) and extract once the right $(\delta_{i+1/2})$ and the left $(\delta_{i-1/2})$ slopes.

## References


[1] R.K. Agarwal, A third-order-accurate upwind scheme for Navier–Stokes solutions at high Reynolds numbers, in: 19th AIAA Aerospace Sciences Meeting, St. Louis, MO, USA, 1981, AIAA paper 1981-112.
[2] W. K Anderson, ThomasJ. L, B. VanLeer, Comparison of finite volume flux vector splitting for the Euler equations, AIAA J. 24 (9) (1986) 1453–1460.
[3] M. Arora, P.L. Roe, A well-balanced TVD limiter for high-resolution calculations of unsteady flow, J. Comput. Phys. 132 (1) (1997) 3–11.
[4] R.Artebrant, Reconstruction Techniques and Finite Volume Schemes for Hyperbolic Conservation Laws, Ph.D. Thesis, Doctoral Theses in Mathematical Sciences, Lund University, 2006.
[5] R. Artebrant, H.J. Schroll, Limiter-free third order logarithmic reconstruction, SIAM J. Sci. Comput. 28 (2006) 359–381.
[6] F. Dubois, Nonlinear Interpolation and Total Variation Diminishing Schemes, Rapport de recherche Aerospatiale Escape et Defense, ST/S 46 195, 1990.
[7] S. Gottlieb, C.-W. Shu, Total variation diminishing Runge–Kutta schemes, Math. Comput. 67 (1998) 73–85.
[8] A. Harten, High resolution schemes for hyperbolic conservation laws, J. Comput. Phys. 59 (1983) 357–393.
[9] A. Harten, B. Enquist, S. Osher, S.R. Chakravarthy, Uniformly high order accurate essentially non-oscillatory schemes III, J. Comput. Phys. 71 (1987) 231–303.
[10] H.T. Huynh, Accurate monotone cubic interpolation, SIAM J. Numer. Anal. 30 (1993) 87–100.
[11] JamesM. Hyman, Accurate monotonicity preserving cubic interpolation, SIAM J. Sci. Stat. Comput 4 (1983) 645–654.
[12] G.-S. Jiang, C.-W. Shu, Efficient implementation of weighted ENO schemes, J. Comput. Phys. 126 (1996) 202–228.
[13] B. Koren, A robust upwind discretization method for advection, diffusion and source terms, in: Koren Vreugdenhil (Ed.), Numerical Methods for Advection–Diffusion Problems, Vieweg, Braunschweig, Germany, 1993, pp. 117–138.
[14] L.D. Landau, E.M. Lifshitz, Fluid Mechanics, Course of Theoretical Physics, vol. 6, Pegamon Press, 1982.
[15] R.J. LeVeque, Finite Volume Methods for Hyperbolic Problems, Cambridge Texts in Applied Mathematics (2003).
[16] A. Liska, B. Wendroff, Comparison of several difference schemes on 1D and 2D test problems for Euler equations, SIAM J. Sci. Comput. 25 (2003) 995–1017.
[17] X.-D. Liu, S. Osher, T. Chan, Weighted essentially nonoscillatory schemee, J. Comput. Phys. 115 (1994) 200–212.
[18] A. Marquina, Local hyperbolic reconstruction of numerical fluxes for nonlinear scalar conservation laws, SIAM J. Sci. Comput. 15 (1994) 892–915.
[19] S. Osher, Convergence of generalized MUSCL schemes, SIAM J. Numer. Anal. 22 (1985) 947–961.
[20] C.W. Schulz-Rinne, J.P. Collins, H.M. Glaz, Numerical solution of the Riemann problem for two-dimensional gas dynamics, SIAM J. Sci. Comput. 14 (1993) 1394–1414.
[21] S. Serna, A class of extended limiters applied to piecewise hyperbolic methods, SIAM J. Sci. Comput. 28 (2006) 123–140.
[22] S. Serna Salichs, High Order Accurate Shock Capturing Schemes for Hyperbolic Conservation Laws based on a new Class of Limiters, Ph.D. Thesis, Doctoral Theses in Applied Mathematics, Universitat de Valencia, 2005.
[23] C.-W. Shu, Numerical experiments on the accuracy of ENO and modified ENO schemes, J. Sci. Comput. 5 (1990) 127–149.
[24] C. -W Shu, S. Osher, Efficient implementation of essentially non-oscillatory shock capturing schemes II, J. Comput. Phys. 126 (1989) 32–78.
[25] S.P. Spekreijse, Multigrid solution of monotone second-order discretizations of hyperbolic conservation laws, Math. Comput. 49 (179) (1987) 135–155.
[26] A. Suresh, H.T. Huynh, Accurate monotonicity-preserving schemes with Runge–Kutta time stepping, J. Comput. Phys. 136 (1997) 83–99.
[27] E.F. Toro, Riemann Solvers and Numerical Methods for Fluid Dynamics, second ed., Springer, Berlin, Germany, 1999.
[28] M. Torrilhon, Non-uniform convergence of finite volume schemes for Riemann problems of ideal magnetohydrodynamics, J. Comput. Phys. 192 (2003) 73–94.
[29] M. Torrilhon, D.S. Balsara, High order WENO schemes: investigation on non-uniform convergence for MHD Riemann problems, J. Comput. Phys. 201 (2004) 586–600.
[30] G.D. VanAlbada, B. VanLeer, W.W. Roberts, A comparative study of computational methods in cosmic gas dynamics, Astron. Astrophys. 108 (1982) 76–84.
[31] B. VanLeer, Towards the ultimate conservative difference scheme V: a second–order sequel to Godunov's method, J. Comput. Phys. 32 (1979) 101–136.
[32] M. Čada, M. Torrilhon, R. Jeltsch, Compact third order logarithmic limiting for non-linear hyperbolic conservation laws, in: Sylvie Benzoni-Gavage, Denis Serre (Eds.), Proceedings of the 11th International Conference on Hyperbolic Problems, Lyon, France, Springer, 2008.
[33] V. Venkatakrishnan, On the accuracy of limiters and convergence to steady state solution, in: 31st AIAA Aerospace Sciences Meeting and Exhibit, Reno, NV, USA, 1993. AIAA paper 93-0880.
[34] N.P. Waterson, H. Deconinck, Design principles for bounded higher-order convection schemes – a unified approach, J. Comput. Phys. 224 (2007) 182–207.
[35] P. Woodward, P. Colella, The numerical simulation of two-dimensional fluid flow with strong shocks, J. Comput. Phys. 54 (1984) 115–173.
[36] P. Woodward, P. Colella, The piecewise parabolic method (PPM) for gas-dynamical simulation, J. Comput. Phys. 54 (1984) 101–136.